Benthic Organic Matter Transformation Drives pH and Carbonate Chemistry in Arctic Marine Sediments

Felipe Sales de Freitas[1], Sandra Arndt[2], Katharine Hendry[1], Johan Faust[3], Allyson Tessin[4], and Christian März[5]

[1]University of Bristol
[2]Universit e Libre de Bruxelles
[3]MARUM Center for Marine Environmental Sciences
[4]Kent State University
[5]Leeds University

November 24, 2022

Abstract

The carbonate chemistry of Arctic Ocean seafloor and its vulnerability to ocean acidification remains poorly explored. This limits our ability to quantify how biogeochemical processes and bottom water conditions shape sedimentary carbonate chemistry, and to predict how climate change may affect such biogeochemical processes at the Arctic Ocean seafloor. Here, we employ an integrated model assessment that explicitly resolves benthic pH and carbonate chemistry along a S—N transect in the Barents Sea. We identify the main drivers of observed carbonate dynamics and estimate benthic fluxes of dissolved inorganic carbon and alkalinity to the Arctic Ocean. We explore how bottom water conditions and in-situ organic matter degradation shape these processes and show that organic matter transformation strongly impacts pH and carbonate saturation (Ω) variations. Aerobic organic matter degradation drives a negative pH shift (pH < 7.6) in the upper 2—5 cm, producing $\Omega < 1$. This causes shallow carbonate dissolution, buffering porewater pH to around 8.0. Organic matter degradation via metal oxide (Mn/Fe) reduction pathways further increases pH and carbonate saturation state. At the northern stations, where $\Omega > 5$ at around 10–25 cm, model simulations result in authigenic carbonate precipitation. Furthermore, benthic fluxes of dissolved inorganic carbon (12.5—59.5 µmol cm-2 yr-1) and alkalinity (11.3—63.2 µmol cm-2 yr-1) are 2—3-fold greater in the northern sites due to greater carbonate dissolution. Our assessment is of significant relevance to predict how changes in the Arctic Ocean may shift carbon burial and pH buffering into the next century.

Benthic Organic Matter Transformation Drives pH and Carbonate Chemistry in Arctic Marine Sediments

F. S. Freitas[1, †], S. Arndt[2, †], K. R. Hendry[1], J. C. Faust[3,4], A. C. Tessin[5], C. März[3]

[1] School of Earth Sciences, University of Bristol, Bristol, BS8 1RJ, UK.

[2] BGeosys, Department of Earth and Environmental Sciences, Université Libre de Bruxelles, Brussels, 1050, Belgium.

[3] School of Earth & Environment, University of Leeds, Leeds, LS2 9TJ, UK.

[4] MARUM - Center for Marine Environmental Sciences, University of Bremen, 28359, Bremen, Germany

[5] Department of Geology, Kent State University, Kent, OH, 44242, USA.

Corresponding author: Felipe S. Freitas (felipe.salesdefreitas@bristol.ac.uk)

[†] These authors contributed equally to the manuscript.

Key Points:

- Aerobic organic matter degradation drives shallow porewater pH and carbonate saturation state decrease in the upper 2—5 cm sediment depth.
- Metal oxide pathways and calcite dissolution increase pH and carbonate saturation in deeper sediments, enabling authigenic precipitation.
- Higher benthic fluxes of alkalinity and DIC from South to North reflect greater carbonate dissolution in the northern Barents Sea sites.

Abstract

The carbonate chemistry of Arctic Ocean seafloor and its vulnerability to ocean acidification remains poorly explored. This limits our ability to quantify how biogeochemical processes and bottom water conditions shape sedimentary carbonate chemistry, and to predict how climate change may affect such biogeochemical processes at the Arctic Ocean seafloor. Here, we employ an integrated model assessment that explicitly resolves benthic pH and carbonate chemistry along a S—N transect in the Barents Sea. We identify the main drivers of observed carbonate dynamics and estimate benthic fluxes of dissolved inorganic carbon and alkalinity to the Arctic Ocean. We explore how bottom water conditions and in-situ organic matter degradation shape these processes and show that organic matter transformation strongly impacts pH and carbonate saturation (**Ω**) variations. Aerobic organic matter degradation drives a negative pH shift (pH < 7.6) in the upper 2—5 cm, producing **Ω** < 1. This causes shallow carbonate dissolution, buffering porewater pH to around 8.0. Organic matter degradation via metal oxide (Mn/Fe) reduction pathways further increases pH and carbonate saturation state. At the northern stations, where **Ω** > 5 at around 10–25 cm, model simulations result in authigenic carbonate precipitation. Furthermore, benthic fluxes of dissolved inorganic carbon (12.5—59.5 µmol cm^{-2} yr^{-1}) and alkalinity (11.3—63.2 µmol cm^{-2} yr^{-1}) are 2—3-fold greater in the northern sites due to greater carbonate dissolution. Our assessment is of significant relevance to predict how changes in the Arctic Ocean may shift carbon burial and pH buffering into the next century.

Keywords: Reaction-Transport Model, benthic carbon fluxes, ocean acidification, authigenic $CaCO_3$ precipitation, calcite dissolution, Barents Sea.

Plain Language Summary

The Arctic Ocean seafloor is an important place for long-term storage of carbon, locking it away from the atmosphere and so counteracting anthropogenic greenhouse gas emissions. However, such carbon storage capacity is also vulnerable itself to climate change. This means that we need to understand how carbon is processed, recycled, and packed away in the Arctic seafloor to be able to predict future shifts in Earth's climate. We use the Barents Sea, a shallow Arctic Ocean area situated between Svalbard (west), Norway (south), and Russia (east) to study carbon recycling in the seafloor and to make predictions of possible impacts of climate change. For that, we use a model that computes chemical processes at the seafloor. This model allows us to investigate how organic carbon (remains of dead algae and marine animals deposited in the bottom of the sea) recycling at the seafloor, and saturation state (limit of which carbon particles become soluble) of bottom waters, can impact the dissolution of inorganic carbon (fragments of shells produced by marine organisms), which in turn leads to the release of carbon back to Arctic Ocean waters. Building on these ideas, we then test how possible different environmental conditions arising from climate change could impact carbon storage in the Arctic Ocean seafloor. We find important climate feedbacks in the system, for example that further acidification of bottom waters could reduce inorganic carbon storage, whereas greater deposition and recycling of organic carbon could help to some extent locking inorganic carbon within seafloor. These important results can help scientists and policy makers to find ways of mitigating the effects of climate change in the next decades.

1 Introduction

The Arctic Ocean, in particular seasonally ice-free shelf seas, is highly vulnerable to ocean acidification (OA) due to its large carbon dioxide (CO_2) uptake capacity. It acts as a global hotspot of CO_2 drawdown from the atmosphere due to its permanently cold surface waters, its undersaturation with respect to CO_2, and brine rejection during sea-ice formation that mixes surface CO_2 into deeper layers (Chen & Borges, 2009; Kaltin et al., 2002). Air—sea CO_2 uptake exerts an important control on seawater pH and carbonate saturation state (Ω) (Millero, 2000; Zeebe & Wolf-Gladrow, 2001). Increasing atmospheric CO_2 levels (e.g., by anthropogenic emissions) can induce negative shifts in pH and Ω (Bindoff et al., 2019; Friedlingstein et al., 2019), leading to OA (Doney et al., 2020; Gattuso & Hansson, 2011). In addition to air—sea CO_2 fluxes, the carbonate chemistry of the Arctic Ocean is further modulated by the distribution of water masses with contrasting physico-chemical characteristics, the seasonal sea-ice dynamics, and fluctuations of riverine discharge, permafrost thawing, coastal erosion, and gas hydrate destabilization (Bates & Mathis, 2009; Cai et al., 2010; Else et al., 2013; Middelburg et al., 2020; Semiletov et al., 2016). These processes can contribute to pH and Ω shifts in shallow and deeper water masses, which can become undersaturated with respect to particulate inorganic carbon (PIC) phases, i.e., carbonate minerals (aragonite and calcite) (Millero, 2000; Zeebe & Wolf-Gladrow, 2001). Such saturation changes can negatively impact Arctic ecosystems, in particular carbonate-shelled plankton (Fabry et al., 2008; Guinotte & Fabry, 2008; Kroeker et al., 2010), reducing PIC export to the seafloor (Luo et al., 2016; Y. Zhang et al., 2020), long-term inorganic carbon burial, and redox processes in Arctic Ocean sediments (Gazeau et al., 2014). Currently, the calcite compensation depth is situated at around 4,000 m water depth across most of the Arctic Ocean, whereas aragonite displays a much shallower (2,000 m depth) compensation depth (Jutterström & Anderson, 2005). However, undersaturation of shallower waters with respect to aragonite is already documented in the Beaufort Gyre (Y. Zhang et al., 2020) and across the East Siberian Shelf (Semiletov et al., 2016). Model results further predict an overall shoaling of both aragonite and calcite compensation depths in the Arctic Ocean due to enhanced CO_2 emissions in the next hundred years (Luo et al., 2016).

Changes in the carbonate chemistry of the Arctic Ocean do not exclusively impact the pelagic system. Crucially, and somewhat underexplored in the Arctic, they also exert an influence on the

seafloor. Given the comparably low PIC deposition flux and bottom water pH values found in the Arctic Ocean (Jones et al., 2019; Kostka et al., 1999), a decrease in PIC fluxes would further suppress the buffering capacity of the sediment, with implications for pH and Ω at the sediment-water interface (SWI) (Middelburg, 2019). Evidence shows that acidification of the Arctic Ocean can induce a decrease in sedimentary porewater pH, as well as a further decrease in carbonate deposition with important implications for porewater Ω, and thus dissolved inorganic carbon (DIC) and total alkalinity (TA) dynamics (Gazeau et al., 2014; Jutterström & Anderson, 2005; Steinsund & Hald, 1994). Consequently, Arctic marine sediments can experience a decrease of pH buffering capacity in response to OA (Bates & Mathis, 2009). Laboratory incubation experiments with Arctic marine sediments showed that a decrease of one pH unit in bottom waters (10-fold increase in H^+ concentrations) causes significant dissolution of benthic carbonate, as indicated by enhanced TA effluxes (Gazeau et al., 2014). Yet, benthic inorganic carbon dynamics and porewater pH and saturation state are not only controlled by bottom water carbonate saturation and PIC deposition but are also influenced by the complex and dynamic diagenetic processes within the sediment. These sub-seafloor processes control sediment-water exchange fluxes and burial fluxes, and thus exert a feedback on ocean carbonate chemistry (Krumins et al., 2013; Morse & Mackenzie, 1990; Soetaert et al., 2007).

In marine sediments, there is hardly a biogeochemical process that does not affect the depth evolution of porewater pH through the production or consumption of protolytic species of the carbonate and sulfide systems (Blouet et al., 2021; Jourabchi et al., 2005; Morse & Mackenzie, 1990). However, the influence of each biogeochemical reaction on porewater pH is not only dependent on the production/consumption rates of these protolytic species, but is also controlled by the ambient pH itself (Jourabchi et al., 2005; Soetaert et al., 2007). In marine sediments within a pH range of 6.5—8.5, some key biogeochemical processes involving organic matter (OM) transformation can be summarized as follows (Figure 1). Aerobic reactions (OM degradation coupled to oxygen consumption and re-oxidation of reduced species – e.g., ammonium, dissolved manganese, dissolved iron, hydrogen sulfide – coupled to oxygen) generally produce negative shifts in porewater pH (Soetaert et al., 2007). Consequently, these processes are generally considered the main drivers of carbonate dissolution that usually takes place in the upper, well-mixed sediment layers (Adler et al., 2001; Berelson et al., 1990, 1994; Emerson & Archer, 1990;

Hales et al., 1994; Jahnke et al., 1994, 1997; Jahnke & Jahnke, 2000, 2004). There is also evidence that such metabolic dissolution impacts carbonate contents of Arctic shelf surface sediments (Hulth et al., 1994; Steinsund & Hald, 1994). OM oxidation coupled to manganese and iron (oxyhydr)oxide reduction consumes protolytic species and thus increases the ambient pH (Krumins et al., 2013; Soetaert et al., 2007). Generally, these processes result in TA production and can drive carbonate oversaturation of porewaters (e.g., Berner et al., 1970; Hu & Cai, 2011), which can favor benthic foraminiferal biomineralization (Green & Aller, 2001). In Arctic Ocean slope sediments, Tessin et al. (2020) observed a reversal of porewaters pH trends (decreasing to increasing) at the redox boundary where metal oxide metabolisms replace oxygen-mediated OM degradation. A similar behavior on pH depth profiles was observed in Arctic shelf sediments (Kostka et al., 1999). In contrast to metal oxide metabolic pathways, the influence of organoclastic sulfate reduction (OSR) on porewater pH and Ω is more sensitive to ambient pH conditions. Taken in isolation from other biogeochemical processes, OSR consumes protolytic species at ambient pH ≤ 6.9, but switches to protolytic species production at pH > 6.9 (Blouet et al., 2021; Soetaert et al., 2007). However, when OSR is followed by precipitation and burial of iron sulfide minerals, it results in carbonate oversaturation of porewaters (Rassmann et al., 2020).

Overall, the processes described above show how complex and dynamic the interplay of OM degradation and re-oxidation processes can be at the seafloor, emphasizing the challenges of fully capturing the controls of pH and carbonate chemistry in Arctic sediments. Therefore, systematically understanding which diagenetic processes govern pH and Ω changes and how they respond to changing environmental conditions is fundamental for constraining the present-day carbonate system of the Arctic seafloor, and for enabling us to assess its potential response to projected ecosystem changes (Luo et al., 2016). For example, if OA intensifies (as predicted), will Arctic sediments still act as major sites of carbon burial? Will these sediments retain their pH buffering capacity? How will exchange fluxes between benthic and pelagic compartments be affected? To address these questions, we employ an integrated model assessment that explicitly resolves benthic pH and carbonate chemistry in Barents Sea shelf sediments to quantify carbonate dynamics, identify its main drivers, and understand DIC and TA return to the Arctic Ocean. We investigate five stations (B13—B17; Table 1; Figure 2) along a 30 °E S—N transect (for details, see Faust et al., 2020, 2021; Freitas et al., 2020). We apply a Reaction-Transport Model (RTM)

approach 1) to reproduce the downcore evolution of porewater and sediment depths profiles including carbonate system parameters (pH, DIC, TA, and Ω), 2) to quantify the relative contribution of each biogeochemical reaction to porewater pH, carbonate saturation and carbonate dissolution/precipitation, 3) to quantify benthic effluxes of TA and DIC, and 4) to assess the sensitivity of benthic carbonate dynamics to changing environmental conditions.

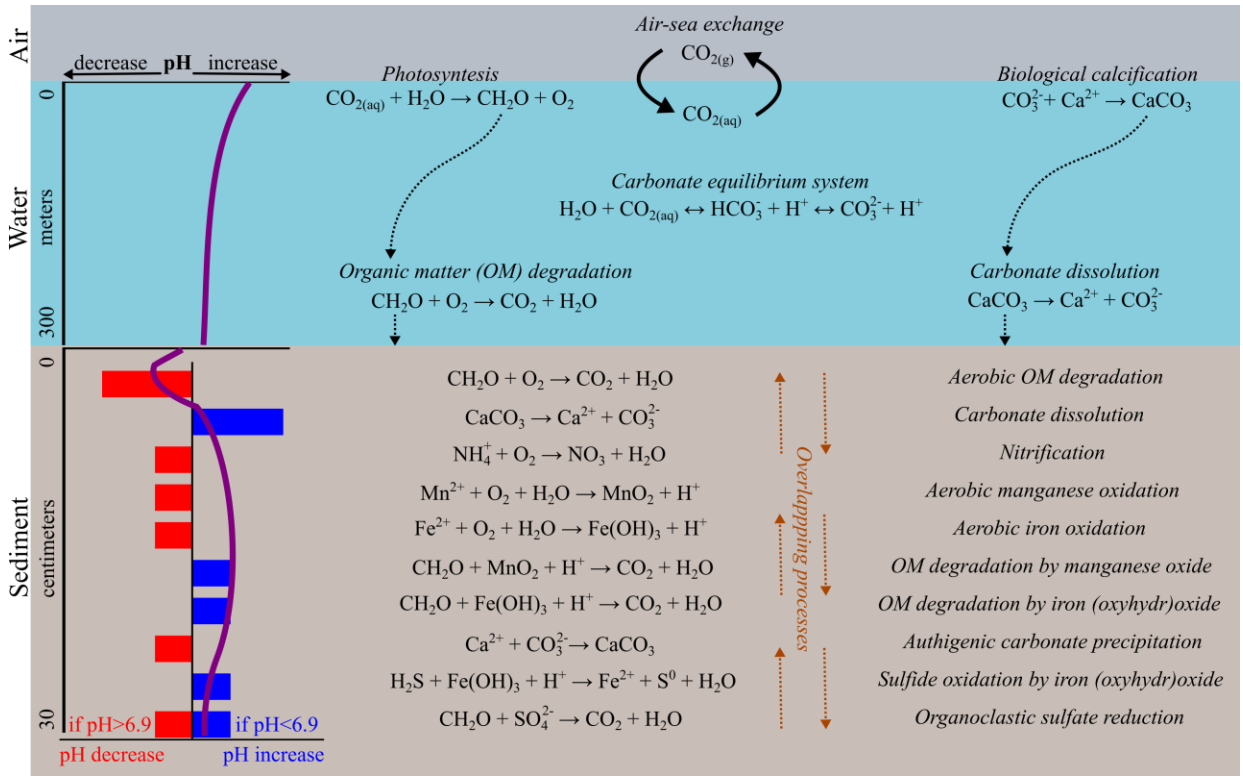

Figure 1. Simplified overview of processes driving carbonate chemistry in marine systems from air (grey box) to water (cyan box) and seafloor (brown box). Reactions are not stoichiometrically balanced and only display key species. For complete reaction network see Table S1. The purple lines illustrate changes in pH profiles as a result of biogeochemical processes. The red bars indicate negative shifts in pH, whereas the blue bars denote positive changes in pH by reactions. Size of bars is not quantitative. Changes in pH are assumed for a typical ambient pH interval of 6.5—8.5. Changes in pH due to organoclastic sulfate reduction can be either positive or negative for the assumed ambient pH interval (see text). Dashed brown arrows indicate that some biogeochemical processes can overlap within sediments. Depicted processes are adapted from Millero (2000) and Soetaert et al. (2007).

2 Methods

2.1 Study area

The Barents Sea (Figure 2) is a shelf area in the Arctic Ocean north of Norway and Russia (Carmack & Wassmann, 2006). The prevailing oceanographic conditions are strongly shaped by sea-ice and wind dynamics, as well as bathymetry. These interactions generate the complex boundary between Arctic Water (ArW; low salinity and low nutrients) and Atlantic Water (AW; high salinity and high nutrients), giving rise to the oceanographic Polar Front (PF) (Oziel et al., 2016). Sea-ice extent during spring—summer periods exerts strong influence on pelagic primary productivity and nutrient cycling, resulting in a general S—N zonation (Dalpadado et al., 2020; Downes et al., 2021; Henley et al., 2020; Lewis et al., 2020; Oziel et al., 2020; Reigstad et al., 2008; Tuerena et al., 2021; Wassmann et al., 2006).

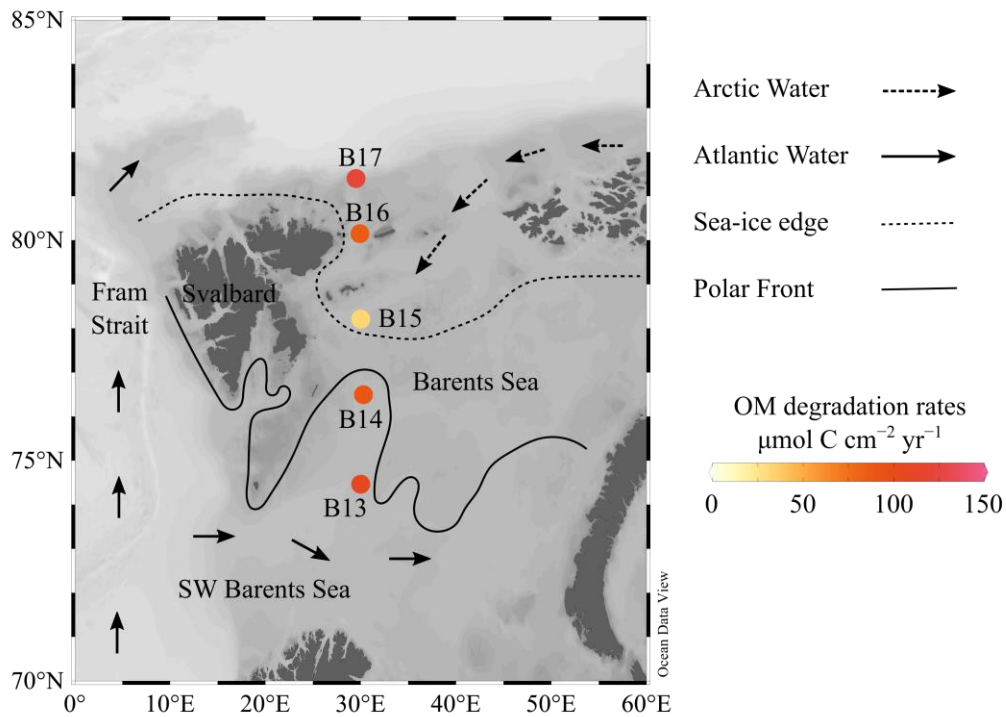

Figure 2. Barents Sea and location of investigated stations (B13—B17) along a 30°E transect. Oceanographic features adapted from Oziel et al. (2016). Organic matter degradation rates are from Freitas et al. (2020). Base map produced with Ocean Data View (Schlitzer, 2021).

The pelagic carbonate chemistry of the Barents Sea is also influenced by latitudinal, bathymetric and sea-ice trends along the shelf (Jones et al., 2019; Tynan et al., 2016). In the SW Barents Sea (71°N—74°N), surface water pH is lower than on the NE shelf (77°N—80°N) where pH reaches up to 8.23. Generally, pH decreases from surface (pH > 8.10) to deep waters (pH < 8.04) along the shelf. Furthermore, surface water pH changes seasonally, with winter values around 8.05 and summer pH > 8.10 (Jones et al., 2019). The TA in the upper layers (shallower than 200 meters) of the SW and S Barents Sea reflects the predominance of warmer and more saline AW, and ranges between 2,310 and 2,330 µM (Jones et al., 2019; Tynan et al., 2016). By contrast, the NE shelf displays the lowest surface (shallower than 50 meters) TA values at 80°N, which reflects both sea-ice melting and biological carbon uptake (Jones et al., 2019).

Sedimentary porewater pH at the sediment-water interface (SWI) is generally lower (pH < 7.70) (Husum et al., 2020; Kostka et al., 1999) as compared to bottom waters (e.g., Jones et al., 2019). TA concentrations at the SWI display a broad range across the Barents Sea and Svalbard shelves. TA concentrations range between 2,060 and 2,690 µM; nevertheless, TA seems to be mostly around 2,350 µM, which includes the Barents Sea slope (north of 81°N) (Hulth et al., 1996). Carbonate contents within the Barents Sea surface sediments reveal higher values on the SW and Norwegian shelves (> 5 wt%), relatively lower contents in the vicinity of the Polar Front (<1.5 wt%) and moderate amounts on the northern shelf (3—5 wt%) (Faust et al., 2020 and references therein). Biogenic calcite is the predominant form of calcium carbonate ($CaCO_3$) across the Barents Sea; dolomite is only present in small amounts and linked to coarse detrital sediment input (Demina et al., 2020; Pautova et al., 2020; Solheim & Elverhoi, 1996).

2.2 Model approach

We adopt the Biogeochemical Reaction Network Simulator (BRNS), a flexible simulation environment suitable for large, mixed kinetic-equilibrium reaction networks (Aguilera et al., 2005; Regnier et al., 2002). We extend the set-up of the BRNS for the Barents Sea sites that was recently applied for investigating and quantifying seafloor OM transformation dynamics (Freitas et al., 2020; Table S1) by explicitly including pH and carbonate dynamics (Sect. 2.2.1) and forcing the model with site-specific SWI conditions for these new variables (Table 1). We do not specifically fit the model to carbonate parameters (pH, DIC, $CaCO_3$), but use the previously calibrated model

set-up to predict seafloor carbonate dynamics. The quality of the model fit to observed carbonate dynamics (Sect. 3.1) thus also offers independent validation for the previously simulated OM dynamics (Freitas et al., 2020). A detailed description of the RTM, including reaction network and boundary condition, can be found in Freitas et al. (2020). Here, we provide a brief description of the newly implemented pH and carbonate system framework, which explicitly resolves downcore evolutions of pH, DIC, and TA. For an overview of parameter values, see Table S1.

2.2.1 pH and carbonate system

Porewater pH (Equation 1), DIC (Equation 2), and TA (Equation 3) are defined as (Millero, 2000; Zeebe & Wolf-Gladrow, 2001):

$$pH = -\log_{10} H^+ \tag{1}$$

$$DIC = CO_2 + HCO_3^- + CO_3^{2-} \tag{2}$$

$$TA = HCO_3^- + 2 \cdot CO_3^{2-} + B(OH)_4^- + HS^- \tag{3}$$

The species accounted in Equation 3 represent the major contributions to porewater TA in porewaters, whereas protons and hydroxyl ions are assumed to be negligible (Jourabchi et al., 2005). Furthermore, bicarbonate (HCO_3^-), carbonate (CO_3^{2-}), and borate ($B(OH)_4^-$) ions account for greater than 99% of TA (e.g., Zeebe & Wolf-Gladrow, 2001).

We assume that calcite is the predominant form of $CaCO_3$ deposited in the Barents Sea sediments (see above; Sect. 2.1). Therefore, we utilize the apparent dissociation constant (K'_{sp}) for calcite (Millero, 1995). The saturation state of calcium carbonates (Ω) is thus controlled by the solubility product for calcite and the apparent thermodynamic constant K'_{sp}, which is a function of pressure, temperature, and salinity.

$$\Omega = \frac{Ca^{2+} \cdot CO_3^{2-}}{K'_{sp}} \tag{4}$$

Ca^{2+} denotes the concentration of dissolved calcium (see Sect. 2.2.2). While we acknowledge that our analyses may underrepresent the contributions of aragonite and dolomite to the benthic pool of $CaCO_3$, we are confident that contribution of these minerals is minimal here based on literature data (e.g., Demina et al., 2020; Pautova et al., 2020; Solheim & Elverhoi, 1996). Calcite dissolution (Equation 5) and authigenic precipitation (Equation 6) are described by a kinetic-thermodynamic rate law with a linear dependency on saturation state (e.g., Morse, 1983):

$$R_{dissolution} = k_{diss} \cdot (1 - \Omega) \cdot Ca^{2+} \cdot CO_3^{2-} \qquad \text{if } \Omega < 1$$
$$R_{dissolution} = 0 \qquad \text{if } \Omega \geq 1 \tag{5}$$

$$R_{precipitation} = k_{prec} \cdot (\Omega - 1) \cdot Ca^{2+} \cdot CO_3^{2-} \qquad \text{if } \Omega \geq 5$$
$$R_{precipitation} = 0 \qquad \text{if } \Omega < 5 \tag{6}$$

where the rate constants for calcite dissolution, k_{diss} and calcite precipitation k_{prec} , are taken from Luff et al. (2000). Our assumption of $\Omega \geq 5$ for calcite precipitation is based on experimental analyses (e.g., Morse et al., 2003; C. Zhang et al., 2010). These have shown that calcite precipitation rates increase at high Ω values due to greater availability of reactants (C. Zhang et al., 2010).

2.2.2 Boundary conditions

Boundary conditions at the SWI are constrained by species concentrations at steady state, while a no-flux condition is specified for all species at the lower boundary (100 cm depth) (for details see Freitas et al., 2020). We use observational data to define species concentrations at the SWI by applying identical boundary conditions to Freitas et al. (2020). Additionally, we adopt site-specific pH values at the SWI determined during a cruise in summer 2018. At stations B14—B17 (Table 1 and S2), downcore porewater pH was determined onboard using a punch-in pH probe (Thermo Scientific Orion Star A329; accuracy 0.002 pH units), which was calibrated prior to measurements

at each site with standard solutions (pH 4.0, 7.0, and 10.0). The depth resolution is 0.5 cm between 0 and 2 cm depth, and 1.0 cm between 2 and 10 cm depth. Since no data are available for B13, a pH value is prescribed for that site following initial sensitivity tests of initial pH values and $CaCO_3$ dissolution rates. We prescribe a TA of 2,350 µM for all sites (Table 1) based on the range of values previously determined by Hulth et al. (1996).

Table 1. Site-specific model parameters prescribed to produce pH and carbonate system downcore evolution.

			Bottom water		Sediment-water interface			
Site	**Lat**	**Depth**	**Temp**	**Sal**	**pH**	**TA**	**$CaCO_3$**	**Ca^{2+}**
	°N	**m**	**°C**			**µM**	**wt%**	**mM**
B17	81.5	291	1.76	34.9	7.20	2,350	3.29	12.6
B16	80.1	294	−1.44	34.7	7.44	2,350	3.88	12.0
B15	78.2	330	−1.49	34.9	7.65	2,350	1.34	12.0
B14	76.5	290	1.95	35.0	7.47	2,350	0.77	11.8
B13	74.5	355	1.77	35.0	7.60	2,350	1.78	12.6

Concentrations of H_2CO_3, HCO_3^-, CO_3^{2-}, $B(OH)_3$, and $B(OH)_4^-$ at the SWI were calculated based on initial pH and TA (Table 1), and corrected for temperature, salinity, and water depth, according to Millero (1995) (Equation 7–15):

$$DIC_{up} = \frac{(TA_{up}+a)\cdot b}{c} \tag{7}$$

$$a = -\frac{k_{eq4}\cdot TB_{up}}{H^+ + k_{eq4}} - \frac{k_{eq3}\cdot TS_{up}}{H^+ + k_{eq3}} - \frac{k_{eq5}}{H^+} + H^+ \tag{8}$$

$$b = 1 + \frac{k_{eq1}}{H^+} + \frac{k_{eq1}+k_{eq2}}{(H^+)^2} \tag{9}$$

$$c = \frac{k_{eq1}}{H^+} + \frac{2\cdot k_{eq1}\cdot k_{eq2}}{(H^+)^2} \tag{10}$$

where TA_{up} denotes TA given in Table 1. DIC_{up}, TB_{up}, and TS_{up} represent SWI carbonate alkalinity, borate alkalinity, and sulfide alkalinity, respectively. We assume TB_{up} of 425 µM and

TS_{up} equal zero. The equilibrium constants (k_{eq1} to k_{eq5}) are calculated according to Millero (1995). Thus,

$$CO_3^{2-} = \frac{TC_{up} \cdot k_{eq1} \cdot k_{eq2}}{(k_{eq1} \cdot k_{eq2}) + (k_{eq1} \cdot H^+) + (H^+)^2} \tag{11}$$

$$HCO_3^- = \frac{TC_{up} \cdot k_{eq1} \cdot H^+}{(k_{eq1} \cdot k_{eq2}) + (k_{eq1} \cdot H^+) + (H^+)^2} \tag{12}$$

$$H_2CO_3 = DIC_{up} - HCO_3^- - CO_3^{2-} \tag{13}$$

$$B(OH)_4^+ = \frac{TB_{up} \cdot H^+}{k_{eq4} + H^+} \tag{14}$$

$$B(OH)_3 = TB_{up} - B(OH)_4^- \tag{15}$$

Contents of $CaCO_3$ at the SWI are from Faust et al. (2020). Porewater Ca concentrations (here assumed to be Ca^{2+}) are from cruise JR16006 (for details see Faust et al., 2020; Freitas et al., 2020).

2.2.3 Controls on pH and Ω

We quantify the relative contributions of diagenetic reactions to changes in pH and Ω following Jourabchi et al. (2005) and Blouet et al. (2021). In short, the influence of each reaction on pH is governed by the mass action laws (Table S1) and fulfils the condition of electric neutrality:

$$\left.\frac{dH^+}{dt}\right|_i = \frac{t_a^i - (\chi_1 + 2\chi_2) t_c^i - t_s^i \sigma_1}{A_1} R^i \tag{16}$$

$$A_1 \equiv DIC \frac{\partial \chi_1}{\partial H^+} + 2DIC \frac{\partial \chi_2}{\partial H^+} + T_S \frac{\partial \sigma_1}{\partial H^+} + T_B \frac{\partial \beta_1}{\partial H^+} - \frac{K_3}{H^{+2}} - 1 \tag{17}$$

Where t_a^i, t_c^i and t_s^i are the stoichiometric coefficients for the production or consumption of alkalinity, DIC and total sulfide, respectively, by a given kinetic reaction i, with rate R^i. The terms

χ_1 and χ_2 are the relative contributions of HCO_3^- and CO_3^{2-} to DIC, respectively, β_1 is the relative contribution of $B(OH)_4^-$ to T_B, and σ_1 is the relative contribution of HS^- to T_S. χ_1, χ_2, σ_1, and β_1 are given by:

$$
\begin{aligned}
HCO_3^- &= \chi_1 DIC \\
CO_3^{2-} &= \chi_2 DIC \\
CO_2 &= \chi_3 DIC \\
HS^- &= \sigma_1 T_S \\
H_2S &= \sigma_2 T_S \\
B(OH)_4^- &= \beta_1 T_B \\
B(OH)_3 &= \beta_2 T_B
\end{aligned}
\tag{18}
$$

and:

$$
\begin{aligned}
\chi_1 &\equiv \frac{K_1^* H^+}{{H^+}^2 + K_1^* H^+ + K_1^* K_2^*} \\
\chi_2 &\equiv \chi_1 \frac{K_2^*}{H^+} \\
\chi_3 &\equiv 1 - \chi_1 - \chi_2 \\
\sigma_1 &\equiv \frac{K_4^*}{K_4^* + H^+} \\
\sigma_2 &\equiv 1 - \sigma_1 \\
\beta_1 &\equiv \frac{K_5^*}{K_5^* + H^+} \\
\beta_2 &\equiv 1 - \beta_1
\end{aligned}
\tag{19}
$$

Following Blouet et al. (2021) and Jourachi et al. (2005), the contribution of a given reaction to changes in saturation state with respect to calcite Ω (Equation 4) can be expressed as a function of their contribution to the production or consumption of calcium and carbonate ions:

$$
\left.\frac{d\Omega}{dt}\right|_i = \frac{1}{K'_{sp}} \left[CO_3^{2-} \left.\frac{dCa^{2+}}{dt}\right|_i + Ca^{2+} \left.\frac{dCO_3^{2-}}{dt}\right|_i \right] \tag{20}
$$

The production or consumption of calcium and carbonate ions can then be expressed as a function of the previously derived rate of change in proton concentrations (Equation 16):

$$\left.\frac{d\Omega}{dt}\right|_i = \frac{1}{K'_{sp}}\left[CO_3^{2-}\left.\frac{dCa^{2+}}{dt}\right|_i + Ca^{2+}\left(t_c^i\chi_2 R^i + T_C\frac{\partial\chi_2}{\partial H^+}\left.\frac{dH^+}{dt}\right|_i\right)\right] \quad (21)$$

Note that since only calcite dissolution and precipitation impact the concentrations of Ca^{2+}, $\frac{dCa^{2+}}{dt}$ is zero for all other reactions.

2.2.4 Benthic-pelagic fluxes of DIC and alkalinity

Steady-state benthic fluxes of DIC ($J_{DIC,Total}$) and TA ($J_{TA,Total}$) across the SWI are calculated based on depth-integrated reaction rates contributing to those fluxes (e.g., Krumins et al., 2013; Table S1):

$$J_{DIC,Total} = J_{DIC,OM} + J_{DIC,Diss} + J_{DIC,Prec} \quad (22)$$

$$J_{TA,Total} = J_{TA,OM} + J_{TA,Diss} + J_{TA,Prec} + J_{TA,H2S} + J_{TA,Fe2+} + J_{TA,Mn2+} + J_{TA,NH4} \quad (23)$$

where the subscript terms *OM*, *Diss*, *Prec*, H_2S, Fe^{2+}, Mn^{2+}, and NH_4 correspond to OM degradation (primary redox reactions), dissolution (calcite and iron sulfide), precipitation of carbonates (calcium, manganese, and iron) and pyrite, sulfide oxidation, iron oxidation, manganese oxidation, and ammonium oxidation, respectively. The relative contributions of each process to DIC and TA fluxes (i.e., stoichiometry and direction – consumption vs. production) are given in Table S1. This approach allows assessing the relative significance of each biogeochemical process producing and consuming DIC and TA to the total SWI flux, and therefore estimating the impacts of specific diagenetic processes on carbonate dynamics at the seafloor.

2.2.5 Sensitivity analyses

Because it is unclear how carbonate chemistry of bottom waters effectively impacts benthic fluxes of DIC and TA (e.g., Gazeau et al., 2014), we performed a parameter sensitivity study to explore

the response of benthic carbonate fluxes to poorly constrained bottom water pH, DIC and TA, as well as to projected future change. We cover a pH interval of 7.0—8.0, which is representative of pH values for the western Barents Sea shelf region (e.g., Husum et al., 2020; Kostka et al., 1999; Tessin et al., 2020; this study). Similarly, we explore a TA range of 2,000—2,700 µM, which is representative for bottom waters and surface sediments of the Barents Sea and Svalbard shelves (Hulth et al., 1996), as well as for the East Siberian Shelf (Miller et al., 2017). All other site-specific model parameters and boundary conditions follow baseline values (Freitas et al., 2020).

We also explore how the effect of changes in input fluxes at the SWI may impact carbonate dynamics at the seafloor. We simulate an overall doubling in sedimentation rates at all sites relative to baseline conditions. Additionally, we test how individual fluctuations of OM, calcite, and metal oxide inputs impact rates of dissolution and precipitation, as well as benthic fluxes of DIC and TA. Here, we prescribe both a halving and a doubling of inputs relative to baseline conditions.

3 Results and Discussion

3.1 Inorganic carbon and pH dynamics along the Barents Sea 30°E south-north transect

Overall, our model results agree well with the observed downcore evolution of measured pH values, as well as $CaCO_3$ contents and porewater Ca^{2+} concentrations (Figure 3). Slight mismatches between observed and simulated Ca^{2+} concentrations at site B13 and B17 most likely result from a slight underestimation of carbonate dissolution rates. Especially at site B13, where bottom water pH has not been measured, lower pH than the one applied might drive a more intense carbonate dissolution in the upper layer.

Observations and simulation results reveal a common pattern in benthic carbonate dynamics. Across the entire transect, the upper, well mixed sediment layers (<5 cm depth) are characterized by low pH and undersaturation of porewaters with respect to calcite, followed by an increase in porewater pH and calcite oversaturation deeper in the sediments. However, the levels of porewater over- and undersaturation, and thus carbonate dissolution and precipitation rates reveal a geographical trend, with decreasing rates from north to south.

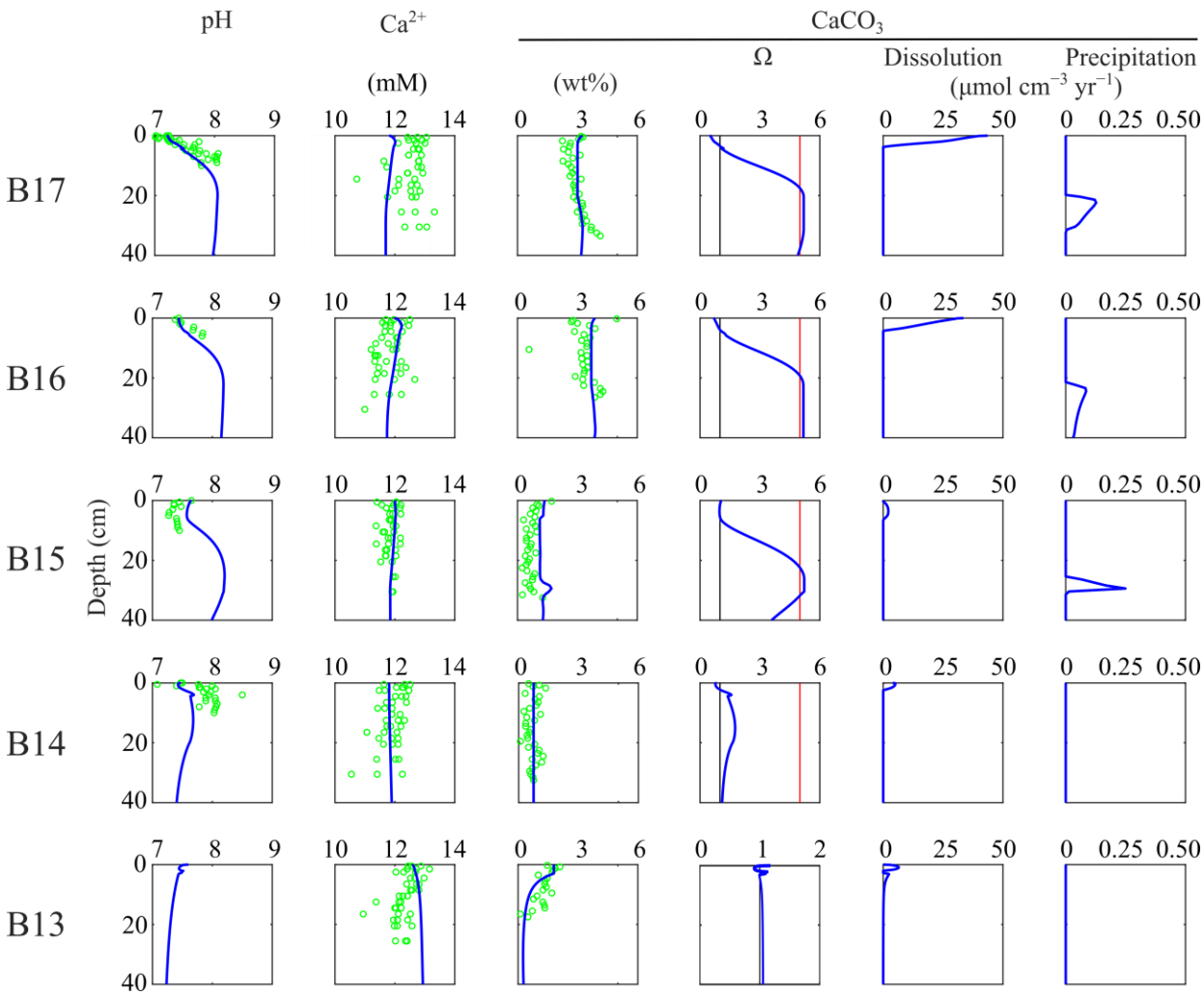

Figure 3. Evolution of pH and carbonate system parameters with sediment depth (in cm) along a 30°E transect in the Barents Sea. Blue lines represent model outputs. Black line on CO_3^{2-} denotes carbonate ions equilibrium. Black and red lines on **Ω** panels denote calcium carbonate saturation (**Ω** = 1) and saturation threshold (**Ω** ≥ 5), respectively. Green circles represent observations (see text for references).

At the northern part of the transect (B16—B17), bottom waters are characterized by low pH (pH < 7.45) and undersaturation with respect to calcite (**Ω** = 0.48—0.68). The shallowest sediment layers reveal high carbonate dissolution rates (Equation 5; $R_{dissolution}$ > 25 μmol cm^{-2} yr^{-1} at the SWI) which coincide with an increase in Ca^{2+} concentrations and a decrease in $CaCO_3$ contents close to the SWI (Figure 3). At the southern part of the transect (B13—B15), bottom water pH (pH > 7.45) and saturation state (**Ω** ≈ 1) are higher, but benthic carbonate contents are lower than

in the northern part stations (Figure 3). Consequently, upper sediment carbonate dissolution is approximately 10-fold lower.

The S—N trend in the intensity of porewater undersaturation and dissolution rates is mirrored by the intensity of porewater oversaturation and carbonate precipitation rates below the well-mixed layer. At the northern part of the transect (B16—B17), porewater pH and Ω increase downwards to broad mid-core (10—20 cm) maxima of pH > 8.0 and Ω > 5, while the southern part of the transect (B13—B14) reveals increasingly lower and more localized mid-depth (5—20 cm) pH and Ω maxima of pH = 7.4—7.6 and Ω = 1.0—1.7. At the southernmost station (B13), porewater pH decreases from 7.6 at the SWI with only a very weakly pronounced and very narrow reversal around 2 cm depth (Figure 3). Porewater calcite saturation thus remains relatively constant, close to unsaturated conditions throughout the simulated sediment column due to a near-complete consumption (i.e., dissolution) of the low sediment carbonate contents and the resulting decrease in buffering capacity. Thus, unfavorable conditions for carbonate precipitation prevail, which could explain the mismatch between model results and analytical data for Ca^{2+}.

Rates of authigenic carbonate precipitation are two orders of magnitude lower than those of dissolution; therefore, model-derived authigenic carbonate precipitation only modestly affects Ca^{2+} and $CaCO_3$ contents at depth. We assess the impact of the Ω threshold on precipitation, and thus precipitation rates, on simulated benthic profiles by assuming a threshold of Ω ≥ 1 for authigenic precipitation (Figure S1). Although these test results lead to a significant increase in precipitation, they also produce further mismatches between model and data depth profiles (Figure S1). Thus, we maintain our relatively conservative threshold of Ω ≥ 5 (Sect. 2.2.1) for authigenic carbonate precipitation.

3.2 Main drivers of inorganic carbon and pH dynamics along the Barents Sea 30°E transect

Within the upper, well-mixed sediment layers (< 5 cm), pH and Ω dynamics are mainly driven by the balance between aerobic degradation of OM and calcite (Figure 4 and 5). At the northern sites (B16—B17), intense aerobic OM degradation supports high rates of proton production (1—2 µmol H^+ cm^{-3} (porewater) yr^{-1}; Figure 4). The resulting decrease in pH and porewater Ω is

counterbalanced by the dissolution of calcium carbonate (Figure 5). Because bottom waters are corrosive (pH < 7.45; Ω < 1) and calcite contents are not limiting ($CaCO_3$ > 3 wt%) in this part of the Barents Sea (Faust et al., 2020), the positive effect of dissolution rates on pH and Ω exceeds the negative effect of aerobic OM degradation (Figure 5). In contrast, at the southernmost sites (B13—B15), higher bottom water pH (pH > 7.45) and a saturation of bottom waters with respect to calcium carbonate (Ω ≈ 1) in combination with lower carbonate contents ($CaCO_3$ < 2 wt%) (Faust et al., 2020) limit the influence of carbonate dissolution on pH and Ω. Consequently, aerobic OM degradation drives an initial decrease in pH and Ω from bottom water values to a local minimum just below the SWI (Figure 4 and 5). Because the apparent OM reactivity, and thus the OM degradation rate is lowest at site B15 (Freitas et al., 2020), the effect of aerobic OM degradation rates on pH and Ω is lowest.

Below the mixed layer (5—10 cm), metal oxide (MnO_2 and $Fe(OH)_3$) reduction exerts an important control on pH and Ω. Often in combination with the oxidation of sulfide by iron (oxyhydr)oxides, the metal oxidation pathways consume H^+ (with maxima rates of −1.0—−0.5 µmol cm^{-3} yr^{-1} of H^+), thus increasing pH values (Figure 4). These processes produce local pH maxima and drive porewaters to oversaturation. The impacts of metal oxide pathways on both pH and Ω are largest at sites B13, B14, B16, and B17, where OM degradation rates are highest. At site B15, sulfide oxidation by iron (oxyhydr)oxides also drives pH and Ω maxima; however, the rates of change are comparatively lower in this station due to generally lower rates of OM degradation (Figure 2; Freitas et al., 2020). At the northern sites, positive changes in Ω are sufficiently large to enable authigenic carbonate precipitation (Ω > 5) at 25—40 cm (Figure 3 and 5). By contrast, reoxidation of Mn^{2+} and Fe^{2+} by O_2 results in intense proton production at B17, resulting in a subsurface negative shift in Ω (−0.02 yr^{-1}). Nevertheless, H^+ increase is buffered by proton consumption yielded by calcite dissolution and metal oxides reduction.

In deeper sediment layers (>10 cm), authigenic precipitation of carbonate minerals ($MnCO_3$, $FeCO_3$, and $CaCO_3$) results in proton production, and thus a drop in pH (Jourabchi et al., 2005; Soetaert et al., 2007). Consequently, Ω also decreases in response to authigenic precipitation. However, because process rates are 1—2 orders of magnitude slower than those of the processes outlined above, authigenic carbonate precipitation only represents a minor control on pH and Ω

within the investigated sediment depths, and total amounts of authigenic carbonate are likely negligible. OSR and nitrification further drive negative changes in Ω. However, the effect these processes in Ω shifts are of relatively minor importance.

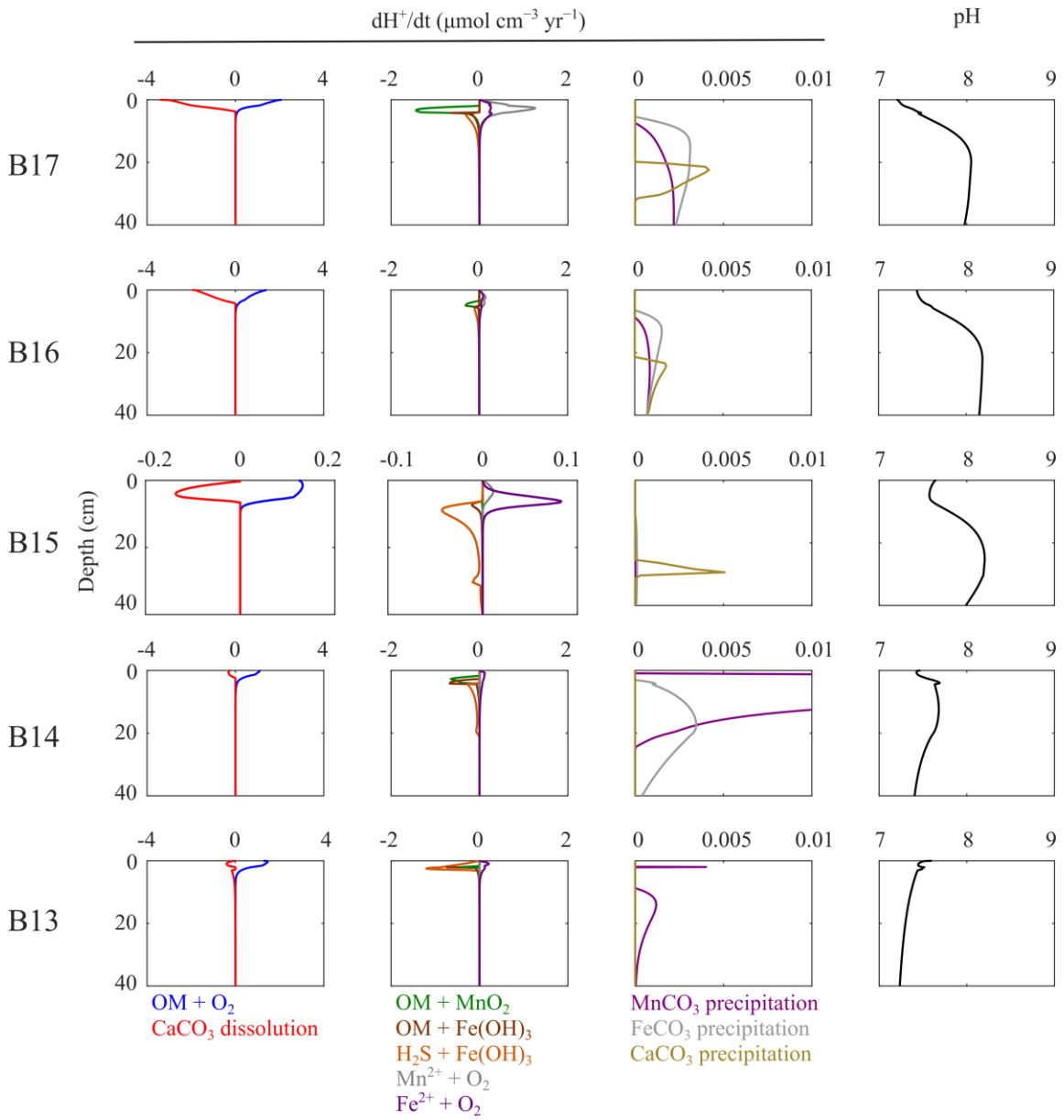

Figure 4. Biogeochemical processes controlling sedimentary evolution of pH with depth. Note that rates of proton production (consumption) (Equation 16) result in a decrease (increase) in porewater pH (Blouet et al., 2021). Also note different x-axis scales in B15 (middle row).

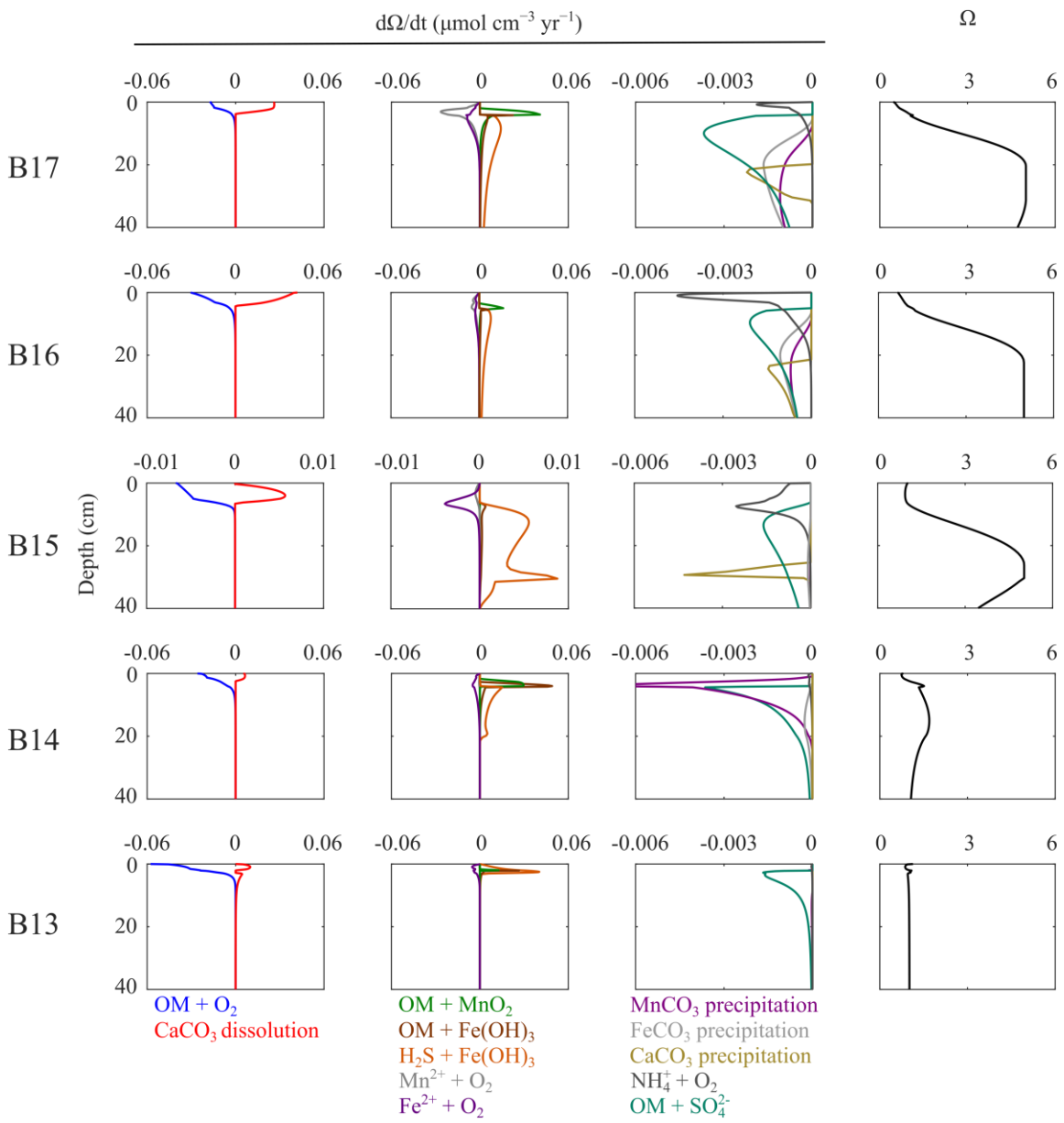

Figure 5. Biogeochemical processes controlling sedimentary evolution of **Ω** with depth. Note different x-axis scales in B15 (middle row).

Model results thus reveal that benthic carbonate dynamics are mainly controlled by a combination of bottom water conditions (pH, **Ω**, and calcite availability) and OM degradation within the sediment. At the northern sites, higher surface ocean pH values >8.1 that only weakly decrease to 8.0 in waters deeper than 300 m (Jones et al., 2019) favor $CaCO_3$ export through the water column to the seafloor, resulting in the relatively high $CaCO_3$ contents preserved in those sediments (Faust et al., 2020). By contrast, the deposition of highly reactive OM supports high OM degradation

rates in the upper sediment layers, driving low pH conditions in both bottom waters (Steinsund & Hald, 1994) and sediment layers directly below the SWI (pH = 7.45—7.65; Freitas et al., 2020). The resulting metabolic dissolution of the deposited $CaCO_3$ results in efficient pH buffering and an increase in Ω, which is further promoted by metal oxide pathways (e.g., Jourabchi et al., 2005; Soetaert et al., 2007). These processes enable deeper authigenic carbonate precipitation at the northern sites. In contrast, at the southern-central parts of the transect, lower carbonate contents at the seafloor (Faust et al., 2020) in combination with equally high rates of (aerobic) OM degradation (Freitas et al., 2020) (except for site B15) result in lower porewaters and bottom water pH at the SWI (pH < 7.45). Since calcite availability limits calcite dissolution (Figure 3), seafloor buffering capacity of porewaters never reaches saturation states that would allow for authigenic precipitation (Ω > 5). Therefore, results indicate that oceanographic conditions (e.g., Oziel et al., 2016) alone cannot directly account for the observed porewater trends.

3.3 Benthic DIC and alkalinity fluxes

Net benthic DIC fluxes from the sediment into the overlying water column range from 12.5 to 59.5 µmol cm^{-2} yr^{-1} and display a clear S—N difference (Figure 6). Relatively lower $J_{DIC,Total}$ are calculated for the southern-central sites (B13—B15), while higher DIC effluxes are quantified at the northern B16—B17 areas ($J_{DIC,Total}$ > 50 µmol cm^{-2} yr^{-1}). At B13—B15, DIC fluxes are predominantly supported by heterotrophic OM degradation (mostly aerobic OM degradation and OSR; Figure S2), while at the northern areas, calcite dissolution further enhances the OM degradation-driven DIC flux and supports nearly one-third of $J_{DIC,Total}$ ($J_{DIC,Diss}$ = 20.1—21.9 µmol cm^{-2} yr^{-1}). At B16—B17, authigenic carbonate precipitation deeper in the sediments acts as a DIC sink ($J_{DIC,Prec}$ = −3.8—−6.8 µmol DIC cm^{-2} yr^{-1}) where Ω > 5 (Figure 2 and 4) enables authigenic calcium carbonate precipitation, but this only exerts a small effect on DIC fluxes. Overall, benthic DIC production at the Barents Sea shelf sediments (ca. 300 m depth) is one order of magnitude lower than DIC production predicted for low latitude, shallow shelf (25—150 m depth) environments at a global scale (Krumins et al., 2013). Such difference is likely associated with the strongly seasonal and limited input of reactive OM to the Barents Sea seafloor (Morata & Renaud, 2008; Reigstad et al., 2008; Wassmann et al., 2004) as compared to the more continuous input of comparably reactive OM in other coastal settings that fuel consistently higher OM degradation rates. For instance, Krumins et al. (2013) assume large fluxes (2.32—6.46 mol C m^{-2}

yr^{-1}) of highly reactive OM (first order degradation rate, k = 0.1—1.0 yr^{-1}) for coastal shelf sediments, whose degradation supports a large DIC production within the sediment.

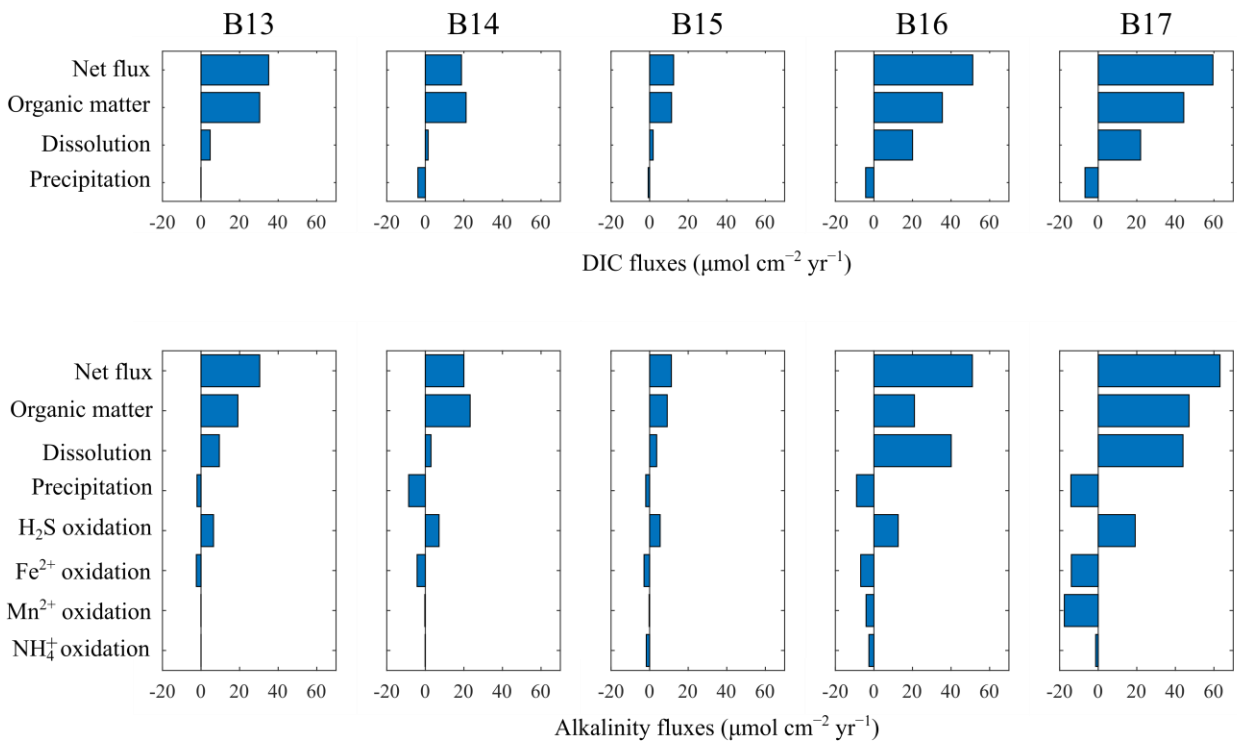

Figure 6. Benthic effluxes of alkalinity (top row) and DIC (bottom row) derived from representative scenarios for Barents Sea. Fluxes are given as total net fluxes across the SWI (positive at all sites), and these are further partitioned by the contribution of each diagenetic process to production (positive values) and consumption (negative values) of alkalinity and DIC.

Net TA benthic fluxes mirror the simulated DIC pattern (Figure 6), i.e., with higher $J_{TA,Total}$ at the northern sites ($J_{TA,Total}$ = 51.1—63.2 μmol cm^{-2} yr^{-1}) than in the southern areas ($J_{TA,Total}$ = 11.3—30.4 μmol cm^{-2} yr^{-1}). At B13—B15, heterotrophic OM degradation represents the main source of alkalinity (predominantly from OSR; Figure S2). Additionally, calcite dissolution and sulfide oxidation by iron (oxyhydr)oxides further add to the TA pool. By contrast, carbonate and pyrite precipitation as well as aerobic iron oxidation only consume minor amounts of TA. At the northern sites, calcite dissolution plays a much larger role in producing alkalinity ($J_{TA,Diss}$ = 40.1—43.9 μmol cm^{-2} yr^{-1}). At B17, calcite dissolution nearly contributes as much as OM degradation to the TA production/flux; while at B16, the contribution of calcite dissolution to the

TA production/flux is 2-fold higher than OM degradation. Additionally, sulfide oxidation (by iron (oxyhydr)oxides) becomes more important for TA production ($J_{TA,H2S}$ = 12.6—19.2 µmol cm^{-2} yr^{-1}). In contrast, mineral precipitation ($J_{TA,Prec}$ = −9.0—−14.2 µmol cm^{-2} yr^{-1}) and aerobic oxidation of dissolved manganese, iron, and ammonium ($J_{TA,Mn2+}$ + $J_{TA,Fe2+}$ + $J_{TA,NH4}$ = −13.5—−32.8 µmol cm^{-2} yr^{-1}) consumes large amounts of porewater alkalinity due to the higher relative contribution of these biogeochemical processes than at the southern sites. Site B17 (and B16 to a lesser extent) displays high rates of OM degradation (Figure 2), of which nearly half is coupled to MnO_2 reduction and OSR, resulting in high production rates of Mn^{2+} and HS^{-}. Here, sulfide oxidation is mostly coupled to iron (oxyhydr)oxide reduction, which produces Fe^{2+}. Further, the product Mn^{2+} and Fe^{2+} are oxidized by oxygen (Freitas et al., 2020).

Generally, simulated $J_{TA,Total}$ falls at the lower end of globally observed values (Table 2). However, global seafloor TA fluxes are highly variable due to factors that include the nature of the OM input, redox conditions in overlying waters and below the seafloor, and depositional rates. Additionally, methodologies vary, with in situ benthic chamber incubations being the most common way of deriving these fluxes (Table 2). Therefore, establishing meaningful comparisons with our estimates must be done with a certain degree of caution to account for these factors. Overall, our estimated net $J_{TA,Total}$ values are similar to TA fluxes determined in the deep Equatorial Pacific, where overlying waters are highly productive (Berelson et al., 1990, 1994), and the Equatorial North Atlantic, where sedimentary carbonate contents are generally high (Jahnke & Jahnke, 2004). Additionally, they are broadly consistent with shelf and slope settings found along the California margin (Berelson et al., 1987; Jahnke et al., 1997) and the Gulf of Mexico shelf/slope (Berelson et al., 2019). These are deep areas (> 790 m) located within highly productive system and exposed to pelagic hypoxic conditions, thus experiencing acidification. Similar order of magnitude TA fluxes are also reported for shallow parts of the California margin (Monterey Bay – 100 m depth) experiencing periods of lowered pelagic productivity, thus decreased OM degradation rates and sediment nutrient efflux (Berelson et al., 2003). By contrast, our $J_{TA,Total}$ estimates are one order of magnitude lower than model-derived, global values for coastal and shelf sediments (Krumins et al., 2013), likely due to the seasonal character of reactive OM input, which is strongly attenuated during settling in the water column (e.g., Reigstad et al., 2008; Wassmann et al., 2004). Furthermore, $J_{TA,Total}$ values for the Barents Sea are significantly lower than TA

fluxes at coastal environments, such as the Rhone delta, where anaerobic oxidation of methane results in high TA production (Rassmann et al., 2020), as well as at estuarine systems in SW Spain (Forja et al., 2004) and the coast of the Gulf of Mexico (Berelson et al., 2019). These areas are heavily influenced by terrestrial and fluvial OM inputs and experience various degrees of anthropogenic impact.

Table 2. Compilation of benthic TA fluxes across contrasting marine systems.

Site	Setting	Depth (m)	OM input	TOC (wt%)	Type	J_{TA}	Unit	Reference
Barents Sea	Shelf	290—355	Pelagic	[a] 1.8—2.5	Model (Steady state)	11.3—63.2	μmol cm^{-2} yr^{-1}	This study [a] (Freitas et al., 2020)
Global	Coast—Shelf	25—150	Pelagic	0.3—0.7	Model (Steady state)	200.7—616.8	μeq cm^{-2} yr^{-1}	(Krumins et al., 2013)
Equatorial Pacific	Abys	4,450—4,910	Pelagic	[b] 0.5—1.0	Chamber (total)	−13.9—36.7	μeq cm^{-2} yr^{-1}	(Berelson et al., 1990) [b] (Jahnke et al., 1982)
Equatorial Pacific	Abys	3,380—4,560	Pelagic	[c] 0.2—1.0	Chamber (total)	13.5—47.8	μeq cm^{-2} yr^{-1}	(Berelson et al., 1994) [c] (Hammond et al., 1996)
Cape Verde Plateau	Abys	3,103	Pelagic	n.a.	Chamber (total)	−1.0—11.0	μeq cm^{-2} yr^{-1}	(Jahnke & Jahnke, 2004)
Ceara Rise	Abys	3,272—4,676	Pelagic	n.a.		−12.9—23.6		
North Carolina depocenter	Slope	750—2,937	Pelagic and lateral transport	1.4—2.7	Chamber (total)	43.3—392.3	μeq cm^{-2} yr^{-1}	(Jahnke & Jahnke, 2000)
California margin	Slope	790—3,745	[d] Pelagic and episodic lateral transport	2.9—3.5	Chamber (total)	54.7—113.2	μeq cm^{-2} yr^{-1}	(Jahnke et al., 1997) [d] (Jahnke et al., 1990)
Southern California	Shelf	900—1,800	Pelagic and episodic lateral transport	3.5—6.0	Chamber (total)	61.7—68.3	μeq cm^{-2} yr^{-1}	(Berelson et al., 1987)
Monterey Bay – California	Shelf	100	Pelagic (upwelling)	0.4—0.5	Chamber (total)	74.8—333.2	μeq cm^{-2} yr^{-1}	(Berelson et al., 2003)
Gulf of Mexico	Coast	16—30	[e] Mixed pelagic and terrestrial	[d] 1.5—1.7	Chamber (total)	240.9—2,701	μeq cm^{-2} yr^{-1}	(Berelson et al., 2019)
	Shelf—Slope	130—1.550	[f] Mainly pelagic	[e] 0.8—1.3		69.4—219.0		

			[e] Minor terrestrial					[e] (Waterson & Canuel, 2008)
								[f] (Morse & Beazley, 2008)
Rhone delta	Coast—Shelf	20—72	Mixed pelagic and terrestrial	1.3—2.0	Chamber (total)	135.1—2,697	µmol cm^{-2} yr^{-1}	(Rassmann et al., 2020)
Tomales Bay – California	Estuary	3—6	Pelagic with terrestrial	n.a.	Chamber (total)	138.7—521.9	µeq cm^{-2} yr^{-1}	(Smith et al., 1987) (Dollar et al., 1991)
Tinto—Odiel System	Estuary	2—5	Mainly terrestrial (inc. anthropogenic) and aquatic	1.1—2.4	Chamber (total)	−10,004—12,592	µmol cm^{-2} yr^{-1}	(Ortega et al., 2008)
Ria de Vigo		4—20		2.9—6.9		4,307—7,516		
Bay of Cadiz		2—14		2.0—2.9		3,869—5,329		
Odiel Estuary	Estuary	3—8	Mainly terrestrial (inc. anthropogenic) and aquatic	1.9—4.2	Chamber (total)	3,613—5,073	µmol cm^{-2} yr^{-1}	(Forja et al., 2004)
Barbete Estuary		3		1.7		4,854		
Palmones Estuary		2—5		0.9—3.4		3,577—4,964		

n.a.: data not available.

3.3 Sensitivity of seafloor carbonate dynamics to varying environmental conditions

Since projected changes in sea-ice and progressive Atlantification (Årthun et al., 2012; Barton et al., 2018; Carmack & Wassmann, 2006; Oziel et al., 2020; Smedsrud et al., 2013) may represent further stressors for seafloor inorganic carbon dynamics, we developed a series of sensitivity experiments (Sect. 2.2.5) to explore the sensitivity of seafloor DIC and TA fluxes to possible fluctuations in environmental conditions. These are not specific projected scenarios for the Barents Sea but are designed to illustrate the potential mechanistic response of the carbonate system in the Barents Sea seafloor to changes in environmental conditions.

3.3.1 Bottom water pH and alkalinity

Despite the plausible range of bottom water TA explored here (e.g., Hulth et al., 1996; Miller et al., 2017), we see that the impact on both TA and DIC fluxes (Figure 7) is generally low (the

isolines are nearly vertical), thus indicating negligible changes regarding bottom water TA within the explored interval. By contrast, along the studied range of pH conditions, we observe far more prominent changes in benthic TA and DIC effluxes. Generally, at pH = 7.0, where more corrosive bottom water conditions prevail, both TA and DIC fluxes are greatest and could reach nearly 100 µmol cm^{-2} yr^{-1} at the northern sites. These trends in $J_{TA,Total}$ and $J_{DIC,Total}$ are further supported by changes in Ω at the SWI (Figure 7). Saturation state largely falls below one at bottom water pH < 7.6, although this threshold gradually shifts to pH < 7.5 at greater bottom water total alkalinity (TA > 2,600 µM).

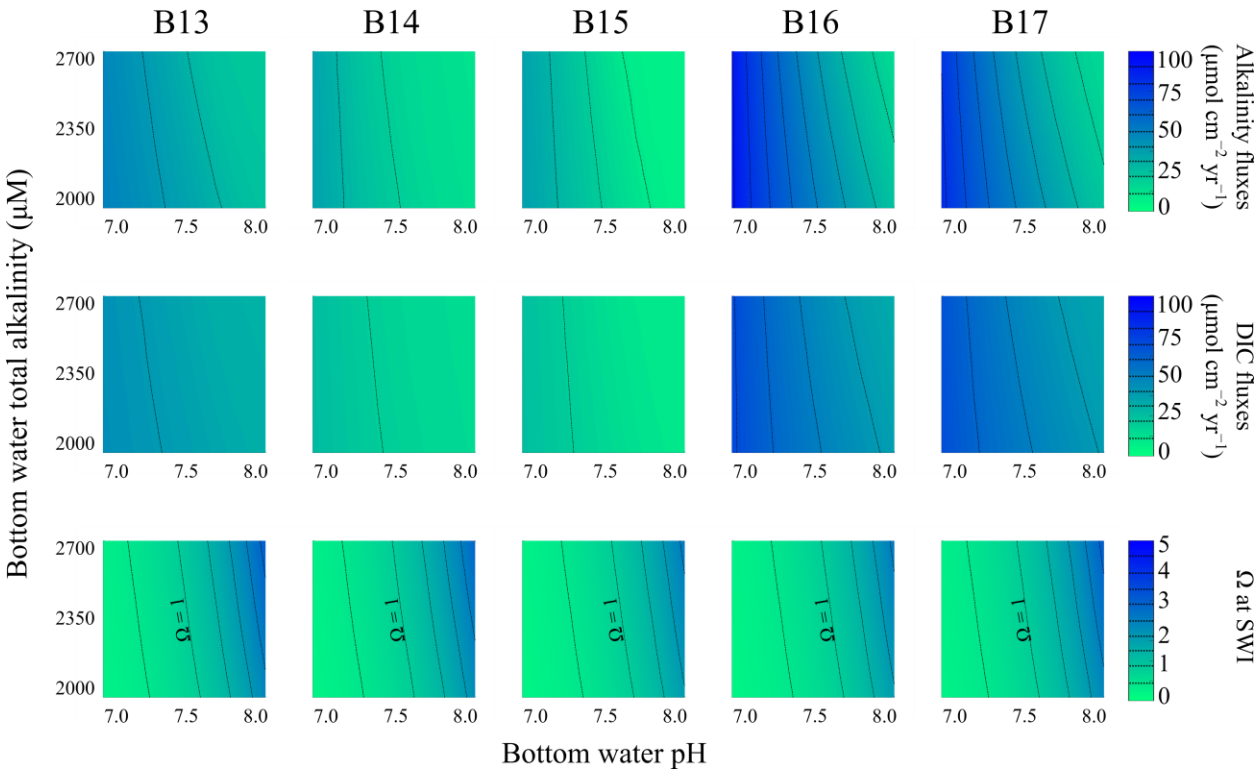

Figure 7. Sensitivity of carbonate chemistry parameters at the seafloor relative to changes in bottom water pH (horizontal axis) and total alkalinity (vertical axis): top row, benthic alkalinity effluxes ($J_{TA,Total}$); middle row, benthic DIC effluxes ($J_{DIC,Total}$); bottom row, Ω at the SWI.

Our model results highlight the role of bottom water pH in further promoting shallow calcium carbonate dissolution and supporting higher DIC and TA fluxes. They agree with laboratory-based experiments which show that low bottom water pH conditions (pH = 7.1) produce large TA effluxes (Gazeau et al., 2014), and field observations that suggest bottom water pH < 7.3 promote

carbonate dissolution at the SWI (Kostka et al., 1999). At pH = 8.0, net effluxes generally decrease, but are higher at high bottom water alkalinity (TA > 2,350 µM).

3.3.2 Particulate export to the seafloor

Although bottom water pH values exert an important influence on the carbonate dynamics, our model results also show that additional environmental conditions such as OM, calcite, and metal oxide contents (Sect. 3.2.2) exert further controls on TA and DIC benthic fluxes along the Barents Sea transect. Thus, we explore how fluctuations of export fluxes to the seafloor may impact carbonate dynamics (Figure 8 and S2; Table S3—S7).

Generally, doubling the sedimentation rates lead to an increase in rates of authigenic precipitation at all sites (Figure 8). However, the magnitudes of these increases differ along the transect. At B13—B15, precipitation rates increase 2—3-fold relative to baseline conditions, whereas at B16—B17 rates are 4—5-fold higher. Results show that higher sedimentation rates trigger a shift in metabolic pathways of OM degradation, such that the relative contribution of aerobic OM degradation decreases (Table S3—S7). This decrease is compensated by increases in metal oxide and OSR contributions, which particularly at B15—B17 leads to an increase in Ω. Consequently, rates of calcite dissolution slightly decrease, while rates of precipitation significantly increase. Except for B13, these changes do not translate into important changes in $J_{DIC,Total}$ and $J_{TA,Total}$. At B13, fluxes increase due to enhanced DIC and TA production by OM degradation and further TA production by sulfide oxidation, which are not offset by limited authigenic carbonate precipitation.

These findings show that changes in OM inputs exert an important influence on carbonate precipitation, and to a lesser extent on dissolution. The latter slightly increases with lower TOC contents at the northern sites. Further, reducing the TOC input to half its baseline value significantly reduces precipitation rates. Lower TOC contents allow a deepening of the oxic layer into the sediments, preventing pH buffering by metal oxide pathways due to generally lower OM degradation rates. Conversely, doubling TOC input leads to a 2—5-fold increase in carbonate precipitation rates at sites B14, B16, B17 relative to baseline conditions. Like the impacts of doubling sedimentation rates, a doubling in TOC results in an overall shift from aerobic to

anaerobic OM degradation, thus promoting Ω oversaturation. Since greater input of OM leads to greater degradation rates (e.g., Freitas et al., 2021), there is an increase in DIC production, and thus benthic fluxes also generally increase despite the DIC sink by authigenic precipitation.

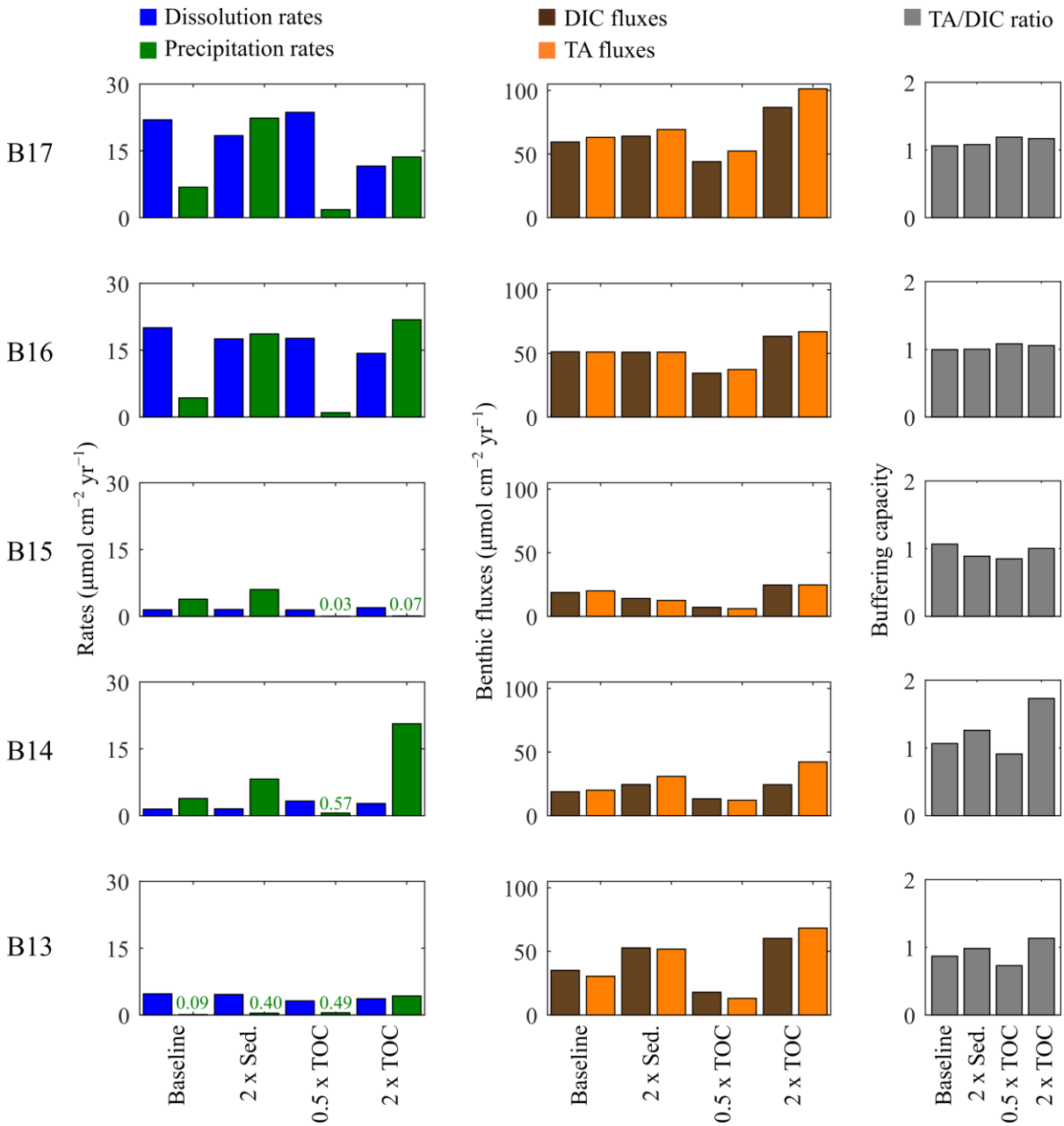

Figure 8. Sensitivity of seafloor carbonate chemistry parameters to changes in sedimentation rates (doubling) and OM inputs (halving and doubling). Left column: rates of dissolution (blue) and precipitation (green). Middle column: benthic fluxes of DIC (brown) and TA (orange). Right column: buffering capacity (grey).

Changes in either metal oxide or calcite inputs to the seafloor exert relatively minor impacts on carbonate dynamics (Figure S2; Table S3—S7). Doubling metal oxide inputs alone results in relatively minor increases in rates of precipitation due to positive impacts on **Ω**. An increase (decrease) in calcite inputs marginally triggers an increase (decrease) in dissolution rates. These impacts are more pronounced at B16—B17, which reflects the influence of higher $CaCO_3$ sedimentary contents at these sites (Faust et al., 2020).

Overall, our analyses do not reveal large changes in the TA/DIC ratios (Figure 8 and S2; Table S3—S7). These are systematically ≤ 1 showing limit changes in sediments buffering capacity against bottom water acidification (e.g., Rabouille et al., 2021). However, we see that doubling sedimentation rates and TOC (Figure 8), especially at B14, results in TA/DIC > 1 due to increased TA alkalinity production by metal oxide pathways, which could locally act as an OA buffer for bottom waters.

4 Conclusions and Implications for a changing Arctic Ocean

Our integrated model approach illustrates the systematic links between inorganic carbon dynamics at the Barents Sea seafloor and benthic OM degradation processes. Further, our analyses show the important role of bottom water conditions in shaping seafloor carbonate chemistry. Importantly, we identify a marked S—N pattern along the Barents Sea 30 °E transect which is defined by the depth evolutions of pH and carbonate saturation state in porewaters, and by benthic fluxes of DIC and alkalinity. Generally, aerobic OM degradation leads to pH and **Ω** decreases in the uppermost sediment layers across the transect. In the northern stations (B16—B17), pH and **Ω** are buffered by calcite dissolution and metal oxide reductive pathways, which enables authigenic carbonate precipitation in deeper sediment layers. These sites are also characterized by high benthic fluxes of DIC and TA. Conversely, pH and **Ω** subsurface buffering is limited in the southern-central sites (B13—B15) and DIC and TA fluxes are 2—3-fold lower. This geographical pattern is strongly shaped by seafloor calcite contents, which are greater at the northern sites (Faust et al., 2020 and references therein), and paralleled by the prevailing water mass and sea-ice gradients along the Barents Sea shelf (e.g., Carmack & Wassmann, 2006). Additionally, our results show that variations in bottom water pH and in OM inputs further impact inorganic carbon dynamics at the

seafloor. When bottom water pH < 7.5, we see a marked increase in DIC and TA benthic fluxes, which is driven by shallow carbonate dissolution. Conversely, we find that enhanced input of OM to the seafloor produces a large increase in carbonate authigenic precipitation, whose impact on benthic fluxes are offset by overall higher production of DIC and TA by OM degradation.

We show systematic links between plausible environmental changes associated to sea-ice loss, Atlantification, and OA and the expected responses of seafloor inorganic carbon dynamics, which are critical because of ongoing changes experienced by the Barents Sea (Årthun et al., 2012; Barton et al., 2018; Oziel et al., 2020; Smedsrud et al., 2013) that are, however, common to the Arctic Ocean in its entirety (Lewis et al., 2020; Luo et al., 2016; Terhaar et al., 2019, 2020; Y. Zhang et al., 2020). For instance, projected shoaling of carbonate compensation depths (Luo et al., 2016) triggered by acidification of the Arctic Ocean will result in marked increase in shallow carbonate dissolution and greater benthic fluxes of DIC and TA (Gazeau et al., 2014), at least where seafloor carbonate contents are capable of sustaining such processes at the expense of PIC burial (Hulth et al., 1994; Steinsund & Hald, 1994). Furthermore, changes in pelagic productivity by Atlantification and/or sea-ice loss (Lewis et al., 2020; Oziel et al., 2020) may shift OM export to the seafloor, thus changing how OM degradation processes control inorganic carbon dynamics within sediments. Such links are crucial for the development of a mechanistic understanding of seafloor carbonate chemistry on the entire Barents Sea shelf. Further, it helps with the development of an informed Pan-Arctic picture of processes governing pH and Ω, as well as carbonate burial and feedbacks to bottom waters for the near future (e.g., end of century), which would complement currently available pelagic assessments (Bindoff et al., 2019; Luo et al., 2016; Meredith et al., 2019; Terhaar et al., 2019, 2020).

Our findings could also impact the application of paleoproxies based on PIC (e.g., on foraminifera, coccolithophores, and pteropods). Model results suggest that these may be impacted by alteration of carbonates within sediments (e.g., Jutterström & Anderson, 2005) when unfavorable conditions for carbonate preservation prevail (e.g., Berelson et al., 1990, 1994; Gazeau et al., 2014; Jahnke et al., 1994, 1997), or condition promote Ω oversaturation (e.g., Berner et al., 1970; Hu & Cai, 2011; Rassmann et al., 2020) and post-depositional overgrowth of tests (e.g., Green & Aller, 2001).

Ultimately, our findings are critical for understanding and trying to mitigate impacts for the future of the Arctic Ocean caused by climate change. This impacts seafloor biogeochemistry (März et al., 2021) and has broader socio-economic implications (Huntington et al., 2021).

Acknowledgments, Samples, and Data

We thank the crew and participants of cruises JR16006 and 17007, RRS *James Clark Ross*, and logistic support from the National Marine Facilities (NMF, Southampton, UK) and the British Antarctic Survey (BAS, Cambridge, UK). This work is part of the Changing Arctic Ocean Seafloor (ChAOS) project, funded by the UKRI-NERC (grant NE/P006493/1 and NE/P005942-1). AT received funding from the European Union's Horizon 2020 research and innovation programme under the Marie Skłodowska-Curie grant agreement No 709175.

We declare no known conflict of interests.

The model employed here is based on Freitas et al. (2020). The updated model code with the implemented pH and carbonate dynamics is available at the GitHub repository (https://github.com/ChangingArcticOceanSeafloorModelling/BarentsSea_BRNS_pH_carbonates last access 10/09/2021).

References

Adler, M., Hensen, C., Wenzhöfer, F., Pfeifer, K., & Schulz, H. D. (2001). Modeling of calcite dissolution by oxic respiration in supralysoclinal deep-sea sediments. *Marine Geology*, *177*(1), 167–189. https://doi.org/10.1016/S0025-3227(01)00130-X

Aguilera, D. R., Jourabchi, P., Spiteri, C., & Regnier, P. (2005). A knowledge-based reactive transport approach for the simulation of biogeochemical dynamics in Earth systems. *Geochemistry, Geophysics, Geosystems*, *6*(7). https://doi.org/10.1029/2004GC000899

Årthun, M., Eldevik, T., Smedsrud, L. H., Skagseth, Ø., & Ingvaldsen, R. B. (2012). Quantifying the Influence of Atlantic Heat on Barents Sea Ice Variability and Retreat. *Journal of Climate*, *25*(13), 4736–4743. https://doi.org/10.1175/JCLI-D-11-00466.1

Barton, B. I., Lenn, Y.-D., & Lique, C. (2018). Observed Atlantification of the Barents Sea Causes the Polar Front to Limit the Expansion of Winter Sea Ice. *Journal of Physical Oceanography*, *48*(8), 1849–1866. https://doi.org/10.1175/JPO-D-18-0003.1

Bates, N. R., & Mathis, J. T. (2009). The Arctic Ocean marine carbon cycle: Evaluation of air-sea CO2 exchanges, ocean acidification impacts and potential feedbacks. *Biogeosciences*, *6*(11), 2433–2459. https://doi.org/10.5194/bg-6-2433-2009

Berelson, W. M., Hammond, D. E., & Cutter, G. A. (1990). In situ measurements of calcium carbonate dissolution rates in deep-sea sediments. *Geochimica et Cosmochimica Acta*, *54*(11), 3013–3020. https://doi.org/10.1016/0016-7037(90)90118-5

Berelson, W. M., Hammond, D. E., & Johnson, K. S. (1987). Benthic fluxes and the cycling of biogenic silica and carbon in two southern California borderland basins. *Geochimica et Cosmochimica Acta*, *51*(6), 1345–1363. https://doi.org/10.1016/0016-7037(87)90320-6

Berelson, W. M., Hammond, D. E., McManus, J., & Kilgore, T. E. (1994). Dissolution kinetics of calcium carbonate in equatorial Pacific sediments. *Global Biogeochemical Cycles*, *8*(2), 219–235. https://doi.org/10.1029/93GB03394

Berelson, W. M., McManus, J., Coale, K., Johnson, K., Burdige, D., Kilgore, T., Colodner, D., Chavez, F., Kudela, R., & Boucher, J. (2003). A time series of benthic flux measurements from Monterey Bay, CA. *Continental Shelf Research*, *23*(5), 457–481. https://doi.org/10.1016/S0278-4343(03)00009-8

Berelson, W. M., McManus, J., Severmann, S., & Rollins, N. (2019). Benthic fluxes from hypoxia-influenced Gulf of Mexico sediments: Impact on bottom water acidification. *Marine Chemistry*, *209*, 94–106. https://doi.org/10.1016/j.marchem.2019.01.004

Berner, R. A., Scott, M. R., & Thomlinson, C. (1970). Carbonate alkalinity in the porewaters of anoxic marine sediments. *Limnology and Oceanography*, *15*(4), 544–549. https://doi.org/10.4319/lo.1970.15.4.0544

Bindoff, N. L., Cheung, W. W. L., Kairo, J. G., Arístegui, J., Guinder, V. A., Hallberg, R., Hilmi, N., Jiao, N., Karim, M. S., O'Donoghue, S., Purca Cuicapusa, S. R., Rinkevich, B., Suga, T., Tagliabue, A., & Williamson, P. (2019). Changing Ocean, Marine Ecosystems, and Dependent Communities. In H.-O. Pörtner, D. C. Roberts, V. Masson-Delmotte, P. Zhai, M. Tignor, E. Poloczanska, K. Mintenbeck, A. Alegría, M. Nicolai, A. Okem, J. Petzold, B. Rama, & N. M. Weyer (Eds.), *IPCC Special Report on the Ocean and Cryosphere in a Changing Climate*. https://www.ipcc.ch/srocc/chapter/chapter-5/

Blouet, J.-P., Arndt, S., Imbert, P., & Regnier, P. (2021). Are seep carbonates quantitative proxies of CH4 leakage? Modeling the influence of sulfate reduction and anaerobic oxidation of methane on pH and carbonate precipitation. *Chemical Geology*, *577*, 120254. https://doi.org/10.1016/j.chemgeo.2021.120254

Cai, W.-J., Chen, L., Chen, B., Gao, Z., Lee, S. H., Chen, J., Pierrot, D., Sullivan, K., Wang, Y., Hu, X., Huang, W.-J., Zhang, Y., Xu, S., Murata, A., Grebmeier, J. M., Jones, E. P., & Zhang, H. (2010). Decrease in the CO_2 Uptake Capacity in an Ice-Free Arctic Ocean Basin. *Science*, *329*(5991), 556. https://doi.org/10.1126/science.1189338

Carmack, E., & Wassmann, P. (2006). Food webs and physical–biological coupling on pan-Arctic shelves: Unifying concepts and comprehensive perspectives. *Progress in Oceanography*, *71*(2–4), 446–477. https://doi.org/10.1016/j.pocean.2006.10.004

Chen, C.-T. A., & Borges, A. V. (2009). Reconciling opposing views on carbon cycling in the coastal ocean: Continental shelves as sinks and near-shore ecosystems as sources of atmospheric CO2. *Surface Ocean CO2 Variability and Vulnerabilities*, *56*(8), 578–590. https://doi.org/10.1016/j.dsr2.2009.01.001

Dalpadado, P., Arrigo, K. R., van Dijken, G. L., Skjoldal, H. R., Bagøien, E., Dolgov, A. V., Prokopchuk, I. P., & Sperfeld, E. (2020). Climate effects on temporal and spatial dynamics of phytoplankton and zooplankton in the Barents Sea. *Progress in Oceanography*, *185*, 102320. https://doi.org/10.1016/j.pocean.2020.102320

Demina, L. L., Dara, O., Aliev, R., Alekseeva, T., Budko, D., Novichkova, E., Politova, N., Solomatina, A., & Bulokhov, A. (2020). Elemental and Mineral Composition of the Barents Sea Recent and Late Pleistocene−Holocene Sediments: A Correlation with Environmental Conditions. *Minerals*, *10*(7), 593. https://doi.org/10.3390/min10070593

Dollar, S. J., Smith, S. V., Vink, S. M., Obrebski, S., & Hollibaugh, J. T. (1991). Annual cycle of benthic nutrient fluxes in Tomales Bay, California, and contribution of the benthos to total ecosystem metabolism. *Marine Ecology Progress Series*, *79*(1/2), 115–125. JSTOR.

Doney, S. C., Busch, D. S., Cooley, S. R., & Kroeker, K. J. (2020). The Impacts of Ocean Acidification on Marine Ecosystems and Reliant Human Communities. *Annual Review of Environment and Resources*, *45*(1), 83–112. https://doi.org/10.1146/annurev-environ-012320-083019

Downes, P. P., Goult, S. J., Woodward, E. M. S., Widdicombe, C. E., Tait, K., & Dixon, J. L. (2021). Phosphorus dynamics in the Barents Sea. *Limnology and Oceanography*, *66*(S1), S326–S342. https://doi.org/10.1002/lno.11602

Else, B. G. T., Galley, R. J., Lansard, B., Barber, D. G., Brown, K., Miller, L. A., Mucci, A., Papakyriakou, T. N., Tremblay, J.-É., & Rysgaard, S. (2013). Further observations of a decreasing atmospheric CO2 uptake capacity in the Canada Basin (Arctic Ocean) due to sea ice loss. *Geophysical Research Letters*, *40*(6), 1132–1137. https://doi.org/10.1002/grl.50268

Emerson, S. R., & Archer, D. (1990). Calcium Carbonate Preservation in the Ocean. *Philosophical Transactions of the Royal Society of London. Series A, Mathematical and Physical Sciences*, *331*(1616), 29–40. JSTOR.

Fabry, V. J., Seibel, B. A., Feely, R. A., & Orr, J. C. (2008). Impacts of ocean acidification on marine fauna and ecosystem processes. *ICES Journal of Marine Science*, *65*(3), 414–432. https://doi.org/10.1093/icesjms/fsn048

Faust, J. C., Stevenson, M. A., Abbott, G. D., Knies, J., Tessin, A., Mannion, I., Ford, A., Hilton, R., Peakall, J., & März, C. (2020). Does Arctic warming reduce preservation of organic matter in Barents Sea sediments? *Philosophical Transactions of the Royal Society A: Mathematical, Physical and Engineering Sciences*, *378*(2181), 20190364. https://doi.org/10.1098/rsta.2019.0364

Faust, J. C., Tessin, A., Fisher, B. J., Zindorf, M., Papadaki, S., Hendry, K. R., Doyle, K. A., & März, C. (2021). Millennial scale persistence of organic carbon bound to iron in Arctic marine sediments. *Nature Communications*, *12*(1), 275. https://doi.org/10.1038/s41467-020-20550-0

Forja, J. M., Ortega, T., DelValls, T. A., & Gómez-Parra, A. (2004). Benthic fluxes of inorganic carbon in shallow coastal ecosystems of the Iberian Peninsula. *Marine Chemistry*, *85*(3–4), 141–156. https://doi.org/10.1016/j.marchem.2003.09.007

Freitas, F. S., Hendry, K. R., Henley, S. F., Faust, J. C., Tessin, A. C., Stevenson, M. A., Abbott, G. D., März, C., & Arndt, S. (2020). Benthic-pelagic coupling in the Barents Sea: An integrated data-model framework. *Philosophical Transactions of the Royal Society A: Mathematical, Physical and Engineering Sciences*, *378*(2181), 20190359. https://doi.org/10.1098/rsta.2019.0359

Freitas, F. S., Pika, P. A., Kasten, S., Jørgensen, B. B., Rassmann, J., Rabouille, C., Thomas, S., Sass, H., Pancost, R. D., & Arndt, S. (2021). New insights into large-scale trends of apparent organic matter reactivity in marine sediments and patterns of benthic carbon transformation. *Biogeosciences*, *18*(15), 4651–4679. https://doi.org/10.5194/bg-18-4651-2021

Friedlingstein, P., Jones, M. W., O'Sullivan, M., Andrew, R. M., Hauck, J., Peters, G. P., Peters, W., Pongratz, J., Sitch, S., Le Quéré, C., Bakker, D. C. E., Canadell, J. G., Ciais, P., Jackson, R. B., Anthoni, P., Barbero, L., Bastos, A., Bastrikov, V., Becker, M., … Zaehle, S. (2019). Global Carbon Budget 2019. *Earth Syst. Sci. Data*, *11*(4), 1783–1838. https://doi.org/10.5194/essd-11-1783-2019

Gattuso, J.-P., & Hansson, L. (Eds.). (2011). *Ocean acidification*. Oxford University Press.

Gazeau, F., van Rijswijk, P., Pozzato, L., & Middelburg, J. J. (2014). Impacts of Ocean Acidification on Sediment Processes in Shallow Waters of the Arctic Ocean. *PLoS ONE*, *9*(4), e94068. https://doi.org/10.1371/journal.pone.0094068

Green, M. A., & Aller, R. C. (2001). Early diagenesis of calcium carbonate in Long Island Sound sediments: Benthic fluxes of Ca2+ and minor elements during seasonal periods of net dissolution. *Journal of Marine Research*, *59*(5), 769–794. https://doi.org/10.1357/002224001762674935

Guinotte, J. M., & Fabry, V. J. (2008). Ocean Acidification and Its Potential Effects on Marine Ecosystems. *Annals of the New York Academy of Sciences*, *1134*(1), 320–342. https://doi.org/10.1196/annals.1439.013

Hales, B., Emerson, S., & Archer, D. (1994). Respiration and dissolution in the sediments of the western North Atlantic: Estimates from models of in situ microelectrode measurements of porewater oxygen and pH. *Deep Sea Research Part I: Oceanographic Research Papers*, *41*(4), 695–719. https://doi.org/10.1016/0967-0637(94)90050-7

Hammond, D. E., McManus, J., Berelson, W. M., Kilgore, T. E., & Pope, R. H. (1996). Early diagenesis of organic material in equatorial Pacific sediments: Stpichiometry and kinetics. *Deep Sea Research Part II: Topical Studies in Oceanography*, *43*(4), 1365–1412. https://doi.org/10.1016/0967-0645(96)00027-6

Henley, S. F., Porter, M., Hobbs, L., Braun, J., Guillaume-Castel, R., Venables, E. J., Dumont, E., & Cottier, F. (2020). Nitrate supply and uptake in the Atlantic Arctic sea ice zone: Seasonal cycle, mechanisms and drivers. *Philosophical Transactions of the Royal Society A: Mathematical, Physical and Engineering Sciences*, *378*(2181), 20190361. https://doi.org/10.1098/rsta.2019.0361

Hu, X., & Cai, W.-J. (2011). An assessment of ocean margin anaerobic processes on oceanic alkalinity budget. *Global Biogeochemical Cycles*, *25*(3). https://doi.org/10.1029/2010GB003859

Hulth, S., Blackburn, T. H., & Hall, P. O. J. (1994). Arctic sediments (Svalbard): Consumption and microdistribution of oxygen. *Marine Chemistry*, *46*(3), 293–316. https://doi.org/10.1016/0304-4203(94)90084-1

Hulth, S., Hall, P. O. J., Landén, A., & Blackburn, T. H. (1996). Arctic sediments (Svalbard): Pore water and solid phase distributions of C, N, P and Si. *Polar Biology*, *16*(6), 447–462. https://doi.org/10.1007/BF02390426

Huntington, H. P., Zagorsky, A., Kaltenborn, B. P., Shin, H. C., Dawson, J., Lukin, M., Dahl, P. E., Guo, P., & Thomas, D. N. (2021). Societal implications of a changing Arctic Ocean. *Ambio*. https://doi.org/10.1007/s13280-021-01601-2

Husum, K., Ninnemann, U., Rydningen, T. A., Alve, E., Altuna, N. E. B., Braaten, A. H., Eilertsen, V. T., Gamboa, V., Kjøller, M. R., Orme, L., Rutledal, S., Tessin, A., & Zindorf, M. (2020). Paleo Cruise 2018. *The Nansen Legacy Report Series*, *3*. https://doi.org/10.7557/nlrs.5502

Jahnke, R. A., Craven, D. B., & Gaillard, J.-F. (1994). The influence of organic matter diagenesis on CaCO3 dissolution at the deep-sea floor. *Geochimica et Cosmochimica Acta*, *58*(13), 2799–2809. https://doi.org/10.1016/0016-7037(94)90115-5

Jahnke, R. A., Craven, D. B., McCorkle, D. C., & Reimers, C. E. (1997). CaCO3 dissolution in California continental margin sediments: The influence of organic matter remineralization. *Geochimica et Cosmochimica Acta*, *61*(17), 3587–3604. https://doi.org/10.1016/S0016-7037(97)00184-1

Jahnke, R. A., Heggie, D., Emerson, S., & Grundmanis, V. (1982). Pore waters of the central Pacific Ocean: Nutrient results. *Earth and Planetary Science Letters*, *61*(2), 233–256. https://doi.org/10.1016/0012-821X(82)90056-5

Jahnke, R. A., & Jahnke, D. B. (2000). Rates of C, N, P and Si recycling and denitrification at the US Mid-Atlantic continental slope depocenter. *Deep Sea Research Part I: Oceanographic Research Papers*, *47*(8), 1405–1428. https://doi.org/10.1016/S0967-0637(99)00118-1

Jahnke, R. A., & Jahnke, D. B. (2004). Calcium carbonate dissolution in deep sea sediments: Reconciling microelectrode, pore water and benthic flux chamber results. *Geochimica et Cosmochimica Acta*, *68*(1), 47–59. https://doi.org/10.1016/S0016-7037(03)00260-6

Jahnke, R. A., Reimers, Clare. E., & Craven, D. B. (1990). Intensification of recycling of organic matter at the sea floor near ocean margins. *Nature*, *348*(6296), 50–54. https://doi.org/10.1038/348050a0

Jones, E., Chierici, M., Skjelvan, I., Norli, M., Børsheim, K. Y., Lødemel, H. H., Sørensen, K., King, A. L., Lauvset, S., Jackson, K., de Lange, T., Johannsessen, T., & Mourgues, C. (2019). *Monitoring ocean acidification in Norwegian seas in 2018* (M–1417).

Jourabchi, P., Van Cappellen, P., & Regnier, P. (2005). Quantitative interpretation of pH distributions in aquatic sediments: A reaction-transport modeling approach. *American Journal of Science*, *305*(9), 919–956. https://doi.org/10.2475/ajs.305.9.919

Jutterström, S., & Anderson, L. G. (2005). The saturation of calcite and aragonite in the Arctic Ocean. *Marine Chemistry*, *94*(1–4), 101–110. https://doi.org/10.1016/j.marchem.2004.08.010

Kaltin, S., Anderson, L. G., Olsson, K., Fransson, A., & Chierici, M. (2002). Uptake of atmospheric carbon dioxide in the Barents Sea. *Seasonal C-Cycling Variability in the Open and Ice-Covered Waters of the Barents Sea*, *38*(1), 31–45. https://doi.org/10.1016/S0924-7963(02)00168-9

Kostka, J. E., Thamdrup, B., Glud, R. N., & Canfield, D. E. (1999). Rates and pathways of carbon oxidation in permanently cold Arctic sediments. *Marine Ecology Progress Series*, *180*, 7–21. JSTOR.

Kroeker, K. J., Kordas, R. L., Crim, R. N., & Singh, G. G. (2010). Meta-analysis reveals negative yet variable effects of ocean acidification on marine organisms. *Ecology Letters*, *13*(11), 1419–1434. https://doi.org/10.1111/j.1461-0248.2010.01518.x

Krumins, V., Gehlen, M., Arndt, S., Van Cappellen, P., & Regnier, P. (2013). Dissolved inorganic carbon and alkalinity fluxes from coastal marine sediments: Model estimates for different shelf environments and sensitivity to global change. *Biogeosciences*, *10*(1), 371–398. https://doi.org/10.5194/bg-10-371-2013

Lewis, K. M., van Dijken, G. L., & Arrigo, K. R. (2020). Changes in phytoplankton concentration now drive increased Arctic Ocean primary production. *Science*, *369*(6500), 198. https://doi.org/10.1126/science.aay8380

Luff, R., Wallmann, K., Grandel, S., & Schlüter, M. (2000). Numerical modeling of benthic processes in the deep Arabian Sea. *Deep Sea Research Part II: Topical Studies in Oceanography*, *47*(14), 3039–3072. https://doi.org/10.1016/S0967-0645(00)00058-8

Luo, Y., Boudreau, B. P., & Mucci, A. (2016). Disparate acidification and calcium carbonate desaturation of deep and shallow waters of the Arctic Ocean. *Nature Communications*, *7*(1), 12821. https://doi.org/10.1038/ncomms12821

März, C., Freitas, F. S., Godbold, J. A., Henley, S. F., Tessin, A. C., Abbott, G. D., Airs, R., Arndt, S., Barnes, D. K. A., Faust, J. C., Grange, L. J., Gray, N. D., Head, I. M., Hendry, K. R., Hilton, R. G., Reed, A. J., Ruhl, S., Solan, M., Souster, T. A., … Widdicombe, S. (2021). Biogeochemical consequences of a changing Arctic shelf seafloor ecosystem. *Ambio*.

Meredith, M., Sommerkorn, M., Cassotta, S., Derksen, C., Ekaykin, A., Hollowed, A., Kofinas, G., Mackintosh, A., Melbourne-Thomas, J., Muelbert, M. M. C., Ottersen, G., Pritchard, H., & Schuur, E. A. G. (2019). Polar Regions. In H.-O. Pörtner, D. C. Roberts, V. Masson-Delmotte, P. Zhai, M. Tignor, E. Poloczanska, K. Mintenbeck, A. Alegría, M. Nicolai, A. Okem, J. Petzold, B. Rama, & Weyer (Eds.), *IPCC Special Report on the Ocean and Cryosphere in a Changing Climate*. https://www.ipcc.ch/srocc/chapter/chapter-3-2/

Middelburg, J. J. (2019). Introduction. In J. J. Middelburg, *Marine Carbon Biogeochemistry* (pp. 1–8). Springer International Publishing. https://doi.org/10.1007/978-3-030-10822-9_1

Middelburg, J. J., Soetaert, K., & Hagens, M. (2020). Ocean Alkalinity, Buffering and Biogeochemical Processes. *Reviews of Geophysics*, *58*(3), e2019RG000681. https://doi.org/10.1029/2019RG000681

Miller, C. M., Dickens, G. R., Jakobsson, M., Johansson, C., Koshurnikov, A., O'Regan, M., Muschitiello, F., Stranne, C., & Mörth, C.-M. (2017). Pore water geochemistry along continental slopes north of the East Siberian Sea: Inference of low methane concentrations. *Biogeosciences*, *14*(12), 2929–2953. https://doi.org/10.5194/bg-14-2929-2017

Millero, F. J. (1995). Thermodynamics of the carbon dioxide system in the oceans. *Geochimica et Cosmochimica Acta*, *59*(4), 661–677. https://doi.org/10.1016/0016-7037(94)00354-O

Millero, F. J. (2000). The Carbonate System in Marine Environments. In A. Gianguzza, E. Pelizetti, & S. Sammartano (Eds.), *Chemical Processes in Marine Environments* (pp. 9–41). Springer Berlin Heidelberg. https://doi.org/10.1007/978-3-662-04207-6_2

Morata, N., & Renaud, P. E. (2008). Sedimentary pigments in the western Barents Sea: A reflection of pelagic–benthic coupling? *Deep Sea Research Part II: Topical Studies in Oceanography*, *55*(20–21), 2381–2389. https://doi.org/10.1016/j.dsr2.2008.05.004

Morse, J. W. (1983). *The kinetics of calcium carbonate dissolution and precipitation* (R. J. Reeder, Ed.; pp. 227–264). De Gruyter. https://doi.org/10.1515/9781501508134-011

Morse, J. W., & Beazley, M. J. (2008). Organic matter in deepwater sediments of the Northern Gulf of Mexico and its relationship to the distribution of benthic organisms. *Deep Sea Research Part II: Topical Studies in Oceanography*, *55*(24–26), 2563–2571. https://doi.org/10.1016/j.dsr2.2008.07.004

Morse, J. W., Gledhill, D. K., & Millero, F. J. (2003). Caco3 precipitation kinetics in waters from the great Bahama bank: *Geochimica et Cosmochimica Acta*, *67*(15), 2819–2826. https://doi.org/10.1016/S0016-7037(03)00103-0

Morse, J. W., & Mackenzie, F. T. (1990). *Geochemistry of sedimentary carbonates*. Elsevier ; Distributors for the U.S. and Canada, Elsevier Science Pub. Co.

Ortega, T., Ponce, R., Forja, J., & Gómez-Parra, A. (2008). Benthic fluxes of dissolved inorganic carbon in the Tinto–Odiel system (SW of Spain). *Continental Shelf Research*, *28*(3), 458–469. https://doi.org/10.1016/j.csr.2007.10.004

Oziel, L., Baudena, A., Ardyna, M., Massicotte, P., Randelhoff, A., Sallée, J.-B., Ingvaldsen, R. B., Devred, E., & Babin, M. (2020). Faster Atlantic currents drive poleward expansion of temperate phytoplankton in the Arctic Ocean. *Nature Communications*, *11*(1), 1705. https://doi.org/10.1038/s41467-020-15485-5

Oziel, L., Sirven, J., & Gascard, J.-C. (2016). The Barents Sea frontal zones and water\hack\newline masses variability (1980–2011). *Ocean Science*, *12*(1), 169–184. https://doi.org/10.5194/os-12-169-2016

Pautova, L. A., Silkin, V. A., Kravchishina, M. D., Chultsova, A. L., & Lisitzin, A. P. (2020). The Biological Calcium Carbonate Pump in the Norwegian and Barents Seas: Regulation Mechanisms. *Doklady Earth Sciences*, *490*(1), 46–50. https://doi.org/10.1134/S1028334X20010079

Rabouille, C., Lansard, B., Owings, S. M., Rabalais, N. N., Bombled, B., Metzger, E., Richirt, J., Eitel, E. M., Boever, A. D., Beckler, J. S., & Taillefert, M. (2021). Early Diagenesis in the Hypoxic and Acidified Zone of the Northern Gulf of Mexico: Is Organic Matter Recycling in Sediments Disconnected From the Water Column? *Frontiers in Marine Science*, *8*, 604330. https://doi.org/10.3389/fmars.2021.604330

Rassmann, J., Eitel, E. M., Lansard, B., Cathalot, C., Brandily, C., Taillefert, M., & Rabouille, C. (2020). Benthic alkalinity and dissolved inorganic carbon fluxes in the Rhône River prodelta generated by decoupled aerobic and anaerobic processes. *Biogeosciences*, *17*(1), 13–33. https://doi.org/10.5194/bg-17-13-2020

Regnier, P., O'Kane, J. P., Steefel, C. I., & Vanderborght, J. P. (2002). Modeling complex multi-component reactive-transport systems: Towards a simulation environment based on the concept of a Knowledge Base. *Applied Mathematical Modelling*, *26*(9), 913–927. https://doi.org/10.1016/S0307-904X(02)00047-1

Reigstad, M., Wexels Riser, C., Wassmann, P., & Ratkova, T. (2008). Vertical export of particulate organic carbon: Attenuation, composition and loss rates in the northern Barents Sea. *Deep Sea Research Part II: Topical Studies in Oceanography*, *55*(20–21), 2308–2319. https://doi.org/10.1016/j.dsr2.2008.05.007

Schlitzer, R. (2021). *Ocean Data View*. odv.awi.de

Semiletov, I., Pipko, I., Gustafsson, Ö., Anderson, L. G., Sergienko, V., Pugach, S., Dudarev, O., Charkin, A., Gukov, A., Bröder, L., Andersson, A., Spivak, E., & Shakhova, N. (2016). Acidification of East Siberian Arctic Shelf waters through addition of freshwater and terrestrial carbon. *Nature Geoscience*, *9*(5), 361–365. https://doi.org/10.1038/ngeo2695

Smedsrud, L. H., Esau, I., Ingvaldsen, R. B., Eldevik, T., Haugan, P. M., Li, C., Lien, V. S., Olsen, A., Omar, A. M., Otterå, O. H., Risebrobakken, B., Sandø, A. B., Semenov, V. A., & Sorokina, S. A. (2013). The role of the Barents Sea in the Arctic climate system. *Reviews of Geophysics*, *51*(3), 415–449. https://doi.org/10.1002/rog.20017

Smith, S. V., Wiebe, W. J., Hollibaugh, J. T., Dollar, S. J., Hager, S. W., Cole, B. E., Tribble, G. W., & Wheeler, P. A. (1987). Stoichiometry of C, N, P, and Si fluxes in a temperate-climate embayment. *Journal of Marine Research*, *45*(2), 427–460. https://doi.org/10.1357/002224087788401124

Soetaert, K., Hofmann, A. F., Middelburg, J. J., Meysman, F. J. R., & Greenwood, J. (2007). The effect of biogeochemical processes on pH. *Marine Chemistry*, *105*(1–2), 30–51. https://doi.org/10.1016/j.marchem.2006.12.012

Solheim, A., & Elverhoi, A. (1996). Surface sediments of the north-western Barents Sea. In R. Stein, G. I. Ivanov, M. A. Levitan, & K. Fahl (Eds.), *Surface-sediment composition and sedimentary processes in the central Arctic Ocean and along the Eurasian Continental Margin*.

Steinsund, P. I., & Hald, M. (1994). Recent calcium carbonate dissolution in the Barents Sea: Paleoceanographic applications. *Marine Geology*, *117*(1), 303–316. https://doi.org/10.1016/0025-3227(94)90022-1

Terhaar, J., Kwiatkowski, L., & Bopp, L. (2020). Emergent constraint on Arctic Ocean acidification in the twenty-first century. *Nature*, *582*(7812), 379–383. https://doi.org/10.1038/s41586-020-2360-3

Terhaar, J., Orr, J. C., Gehlen, M., Ethé, C., & Bopp, L. (2019). Model constraints on the anthropogenic carbon budget of the Arctic Ocean. *Biogeosciences*, *16*(11), 2343–2367. https://doi.org/10.5194/bg-16-2343-2019

Tessin, A., März, C., Blais, M.-A., Brumsack, H.-J., Matthiessen, J., O'Regan, M., & Schnetger, B. (2020). Arctic Continental Margin Sediments as Possible Fe and Mn Sources to Seawater as Sea Ice Retreats: Insights From the Eurasian Margin. *Global Biogeochemical Cycles*, *34*(8), e2020GB006581. https://doi.org/10.1029/2020GB006581

Tuerena, R. E., Hopkins, J., Ganeshram, R. S., Norman, L., de la Vega, C., Jeffreys, R., & Mahaffey, C. (2021). Nitrate assimilation and regeneration in the Barents Sea: Insights from nitrate isotopes. *Biogeosciences*, *18*(2), 637–653. https://doi.org/10.5194/bg-18-637-2021

Tynan, E., Clarke, J. S., Humphreys, M. P., Ribas-Ribas, M., Esposito, M., Rérolle, V. M. C., Schlosser, C., Thorpe, S. E., Tyrrell, T., & Achterberg, E. P. (2016). Physical and biogeochemical controls on the variability in surface pH and calcium carbonate saturation states in the Atlantic sectors of the Arctic and Southern Oceans. *Deep Sea Research Part II: Topical Studies in Oceanography*, *127*, 7–27. https://doi.org/10.1016/j.dsr2.2016.01.001

Wassmann, P., Bauerfeind, E., Fortier, M., Fukuchi, M., Hargrave, B., Moran, B., Noji, T., Nöthig, E.-M., Olli, K., Peinert, R., Sasaki, H., & Shevchenko, V. (2004). Particulate Organic Carbon Flux to the Arctic Ocean Sea Floor. In R. Stein & R. W. MacDonald (Eds.), *The Organic Carbon Cycle in the Arctic Ocean* (pp. 101–138). Springer Berlin Heidelberg. https://doi.org/10.1007/978-3-642-18912-8_5

Wassmann, P., Slagstad, D., Riser, C. W., & Reigstad, M. (2006). Modelling the ecosystem dynamics of the Barents Sea including the marginal ice zone. *Journal of Marine Systems*, *59*(1–2), 1–24. https://doi.org/10.1016/j.jmarsys.2005.05.006

Waterson, E. J., & Canuel, E. A. (2008). Sources of sedimentary organic matter in the Mississippi River and adjacent Gulf of Mexico as revealed by lipid biomarker and δ13CTOC analyses. *Organic Geochemistry*, *39*(4), 422–439. https://doi.org/10.1016/j.orggeochem.2008.01.011

Zeebe, R. E., & Wolf-Gladrow, D. A. (2001). *CO_2 in seawater: Equilibrium, kinetics, isotopes*. Elsevier.

Zhang, C., Dehoff, K., Hess, N., Oostrom, M., Wietsma, T. W., Valocchi, A. J., Fouke, B. W., & Werth, C. J. (2010). Pore-Scale Study of Transverse Mixing Induced CaCO3 Precipitation and Permeability Reduction in a Model Subsurface Sedimentary System. *Environmental Science & Technology*, *44*(20), 7833–7838. https://doi.org/10.1021/es1019788

Zhang, Y., Yamamoto-Kawai, M., & Williams, W. J. (2020). Two Decades of Ocean Acidification in the Surface Waters of the Beaufort Gyre, Arctic Ocean: Effects of Sea Ice Melt and Retreat From 1997–2016. *Geophysical Research Letters*, *47*(3), e60119. https://doi.org/10.1029/2019GL086421

Table S1. Reaction network and parameters controlling the model-derived seafloor dynamics of pH and inorganic carbon in the Barents Sea. Stoichiometric terms x/y/z are defined as 106/12/1 (Freitas et al., 2020). The terms t_a^i, t_c^i, and t_s^i denote the mass action laws and stoichiometric coefficients of total alkalinity, total dissolved inorganic carbon, and total sulfides, respectively (e.g., Blouet et al., 2021; Jourabchi et al., 2005). The terms ΔDIC and ΔTA denote the stoichiometric coefficients of production (positive) and consumption (negative) of benthic-pelagic fluxes of dissolved inorganic carbon and total alkalinity, respectively. γ_N = 1/12 and γ_P = 1/106 (e.g., Soertaet et al., 2007). SD is the volume conversion term ($SD = \frac{1-porosity}{porosity}$) (e.g., Freitas et al., 2020).

	Reaction pathway	t_a^i	t_c^i	t_s^i	**ΔDIC**	**ΔALK**
	Primary redox reactions					
r_1	$(CH_2O)_x(NH_3)_y(H_3PO_4)_z + (x+2y)O_2 + (y+2z)HCO_3^- \rightarrow (x+y+2z)CO_2 + yNH_4^+ + zHPO_4^{2-} + (x+2y+2z)H_2O$	y−2z	1	0	1·SD	$(-\gamma_N-\gamma_P)$·SD
r_2	$(CH_2O)_x(NH_3)_y(H_3PO_4)_z + \left(\frac{4x+3y}{5}\right)NO_3^- \rightarrow \left(\frac{2x+4y}{5}\right)N_2 + \left(\frac{x-3y+10z}{5}\right)CO_2 + \left(\frac{4x+3y-10z}{5}\right)HCO_3^- + zHPO_4^{2-} + \left(\frac{3x+6y+10z}{5}\right)H_2O$	(4+3y−10z)/5	1	0	1·SD	$(4/5+3/5\cdot\gamma_N-\gamma_P)$·SD
r_3	$(CH_2O)_x(NH_3)_y(H_3PO_4)_z + 2\,HR\,MnO_2 + (3x+y-2z)CO_2 + (x+y-2z)H_2O \rightarrow 2Mn^{2+} + (4x+y-2z)HCO_3^- + yNH_4^+ + HPO_4^{2-}$	4+y−2z	1	0	1·SD	$(4+\gamma_N-\gamma_P)$·SD
r_4	$(CH_2O)_x(NH_3)_y(H_3PO_4)_z + 4\,HR\,Fe(OH)_3 + (7x+y-2z)CO_2 \rightarrow 4Fe^{2+} + (8x+y-2z)HCO_3^- + yNH_4^+ + zHPO_4^{2-} + (3x-y+2z)H_2O$	8+y−2z	1	0	1·SD	$(8+\gamma_N-\gamma_P)$·SD
r_5	$(CH_2O)_x(NH_3)_y(H_3PO_4)_z + \frac{x}{2}SO_4^{2-} + (y-2z)CO_2 + (y-2z)H_2O \rightarrow \frac{x}{2}H_2S + (x+y-2z)HCO_3^- + yNH_4^+ + zHPO_4^{2-}$	1+y−2z	1	0.5	1·SD	$(1+\gamma_N-\gamma_P)$·SD
r_6	$(CH_2O)_x(NH_3)_y(H_3PO_4)_z + (y-2z)H_2O \rightarrow \left(\frac{x-2y+4z}{2}\right)CO_2 + (y-2z)HCO_3^- + yNH_4^+ + zHPO_4^{2-} + \frac{x}{2}CH_4$	y−2z	0.5	0	0.5·SD	$(\gamma_N-\gamma_P)$·SD

	Secondary redox reactions					
r_7	$NH_4^+ + 2O_2 + 2HCO_3^- \rightarrow NO_3^- + 2CO_2 + 3H_2O$	−2	0	0	0	−2
r_8	$Mn^{2+} + \frac{1}{2}O_2 + 2HCO_3^- \rightarrow HR\ MnO_2 + 2CO_2 + H_2O$	−2	0	0	0	−2
r_9	$2Fe^{2+} + HR\ MnO_2 + 2HCO_3^- + 2H_2O \rightarrow 2\ HR\ Fe(OH)_3 + Mn^{2+} + 2CO_2$	−2	0	0	0	−2·SD
r_{10}	$2Fe^{2+} + PR\ MnO_2 + 2HCO_3^- + 2H_2O \rightarrow 2\ HR\ Fe(OH)_3 + Mn^{2+} + 2CO_2$	−2	0	0	0	−2·SD
r_{11}	$Fe^{2+} + \frac{1}{4}O_2 + 2HCO_3^- + \frac{1}{2}H_2O \rightarrow HR\ Fe(OH)_3 + 2CO_2$	−2	0	0	0	−2
r_{12}	$H_2S + 2O_2 + 2HCO_3^- \rightarrow SO_4^{2-} + 2CO_2 + 2H_2O$	−2	0	−1	0	−2
r_{13}	$H_2S + HR\ MnO_2 + 2CO_2 \rightarrow Mn^{2+} \rightarrow S^0 + 2HCO_3^-$	2	0	−1	0	2·SD
r_{14}	$H_2S + PR\ MnO_2 + 2CO_2 \rightarrow Mn^{2+} \rightarrow S^0 + 2HCO_3^-$	2	0	−1	0	2·SD
r_{15}	$H_2S + 2\ HR\ Fe(OH)_3 + 4CO_2 \rightarrow 2Fe^{2+} + S^0 + 4HCO_3^- + H_2O$	4	0	−1	0	4·SD
r_{16}	$H_2S + 2\ MR\ Fe(OH)_3 + 4CO_2 \rightarrow 2Fe^{2+} + S^0 + 4HCO_3^- + H_2O$	4	0	−1	0	4·SD
r_{17}	$H_2S + 2\ PR\ Fe(OH)_3 + 4CO_2 \rightarrow 2Fe^{2+} + S^0 + 4HCO_3^- + H_2O$	4	0	−1	0	4·SD
r_{18}	$CH_4 + CO_2 + SO_4^{2-} \rightarrow 2HCO_3^- + H_2S$	2	1	1	1	2
r_{19}	$CH_4 + 2O_2 \rightarrow CO_2 + 2H_2O$	0	1	0	1	0
r_{20}	$FeS + O_2 \rightarrow Fe^{2+}SO_4^{2-}$	0	0	0	0	0

	Other reactions					
r_{21}	$HR\ MnO_2 \rightarrow PR\ MnO_2$	0	0	0	0	0
r_{22}	$HR\ Fe(OH)_3 \rightarrow MR\ Fe(OH)_3$	0	0	0	0	0
	Mineral reactions					
r_{23}	$Mn^{2+} + 2HCO_3^- \rightarrow MnCO_3 + CO_2 + H_2O$	−2	-1	0	−1	−2
r_{24}	$Fe^{2+} + H_2S + 2HCO_3^- \rightarrow FeS + 2CO_2 + 2H_2O$	−2	0	−1	0	−2
r_{25}	$FeS + 2CO_2 + 2H_2O \rightarrow Fe^{2+} + H_2S + 2HCO_3^-$	2	0	1	0	2·SD
r_{26}	$Fe^{2+} + 2HCO_3^- \rightarrow FeCO_3 + CO_2 + H_2O$	−2	−1	0	−1	−2
r_{27}	$FeS + H_2S \rightarrow FeS_2$	0	0	−1	0	0
r_{28}	$3FeS + S^0 \rightarrow Fe_3S_4$	−2	0	3	0	0
r_{29}	$PO_4^{3-} \rightarrow CFA$				0	−2
r_{30}	$CaCO_3 + H^+ \rightarrow Ca^{2+} + HCO_3^-$	2	1	0	1·SD	2·SD
r_{31}	$Ca^{2+} + HCO_3^- \rightarrow CaCO_3$	−2	−1	0	−1	−2
r_{32}	$4S^0 + 4H_2O \rightarrow SO_4^{2-} + 3H_2S + 2H^+$				0	−2

	Equilibria reactions					
r_{33}	$NH_4^+(aq) \rightarrow NH_4^+(ads)$	0	0	0	0	0
r_{34}	$PO_4^{3-}(aq) \rightarrow PO_4^{3-}(ads)$	0	0	0	0	−2
r_{35}	$Fe^{2+}(aq) \rightarrow Fe^{2+}(ads)$	0	0	0	0	0
r_{36}	$Fe(OH)_3 + PO_4^{3-} \rightarrow PO_4(ads_{Fe(OH)3})$	0	0	0	0	−2
r_{37}	$CO_2 + H_2O \rightarrow H^+ + HCO_3^-$	0	0	0	0	0
r_{38}	$HCO_3^- \rightarrow H^+ + CO_3^{2-}$	0	0	0	0	0
r_{39}	$H_2S \rightarrow H^+ + HS^-$	0	0	0	0	0
r_{40}	$B(OH)_3 \rightarrow H^+ + B(OH)_4^-$	0	0	0	0	0

Global Biogeochemical Cycles

Supporting Information for

Benthic Organic Matter Transformation Drives pH and Carbonate Chemistry in Arctic Marine Sediments

F. S. Freitas[1], S. Arndt[2], K. R. Hendry[1], J. C. Faust[3,4], A. C. Tessin[5], C. März[3]

[1]School of Earth Sciences, University of Bristol, Bristol, BS8 1RJ, UK.

[2]BGeosys, Department of Earth and Environmental Sciences, Université Libre de Bruxelles, Brussels, 1050, Belgium.

[3]School of Earth & Environment, University of Leeds, Leeds, LS2 9TJ, UK.

[4] MARUM - Center for Marine Environmental Sciences, University of Bremen, 28359, Bremen, Germany

[5] Department of Geology, Kent State University, Kent, OH, 44242, USA.

Contents of this file

Additional Supporting Information (Files uploaded separately)

Figures

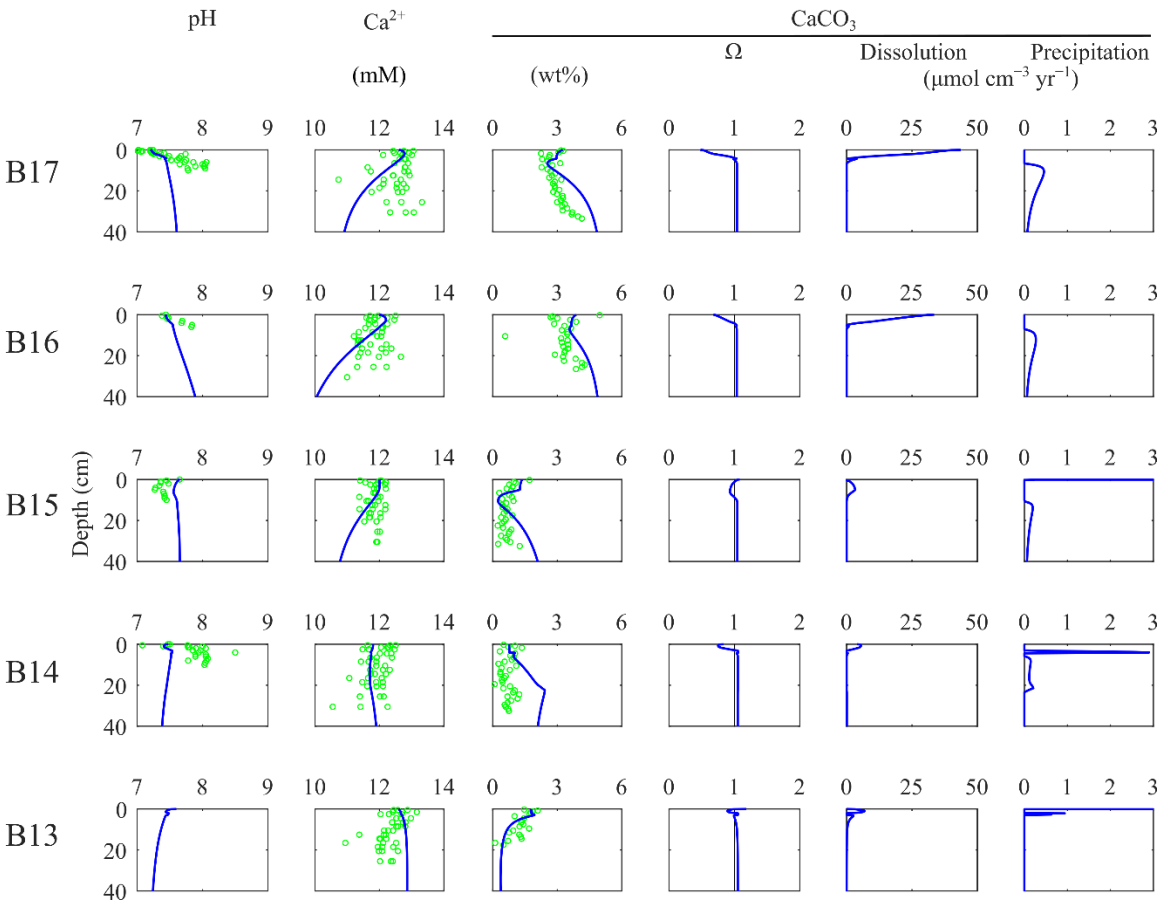

Figure S1. Evolution of pH and carbonate system parameters with depth (in cm) along a 30°E transect in the Barents Sea assuming a threshold of $\Omega \geq 1$ for authigenic $CaCO_3$ precipitation. Blue lines represent model outputs and green circles denote observation (see main text).

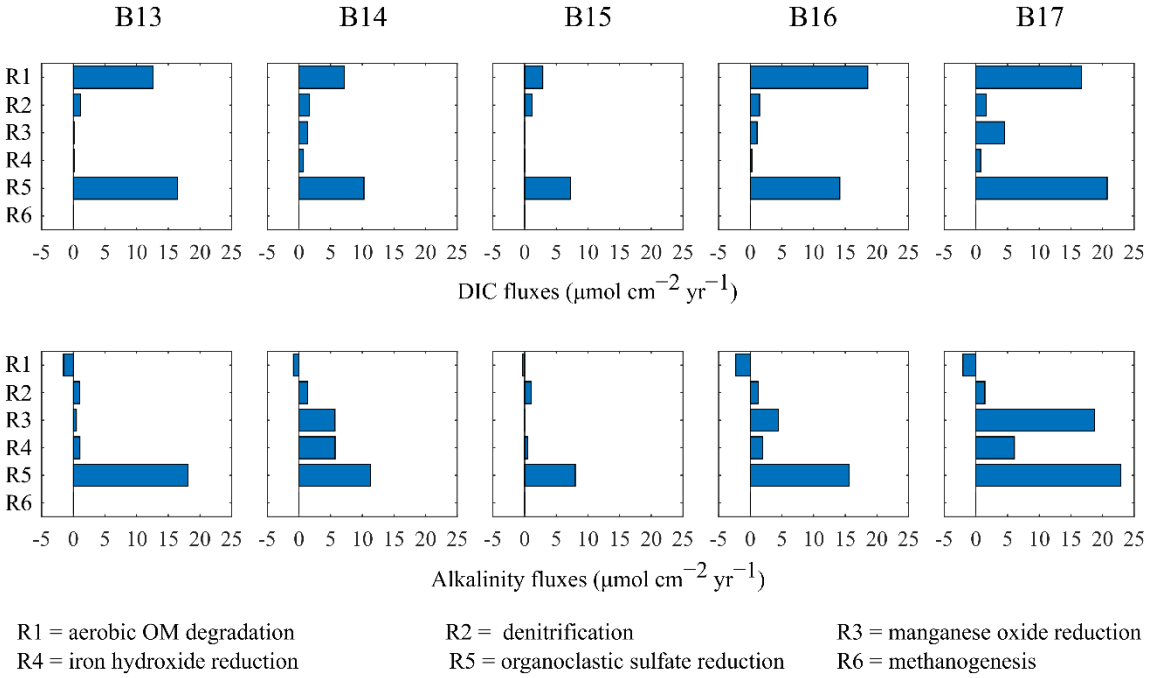

R1 = aerobic OM degradation
R2 = denitrification
R3 = manganese oxide reduction
R4 = iron hydroxide reduction
R5 = organoclastic sulfate reduction
R6 = methanogenesis

Figure S2. Benthic fluxes of DIC (top row) and alkalinity (bottom row) derived from organic matter degradation pathways (primary redox reaction) along the 30°E transect in the Barents Sea. Positive fluxes indicate production and negative fluxes denote consumption by each degradation pathway.

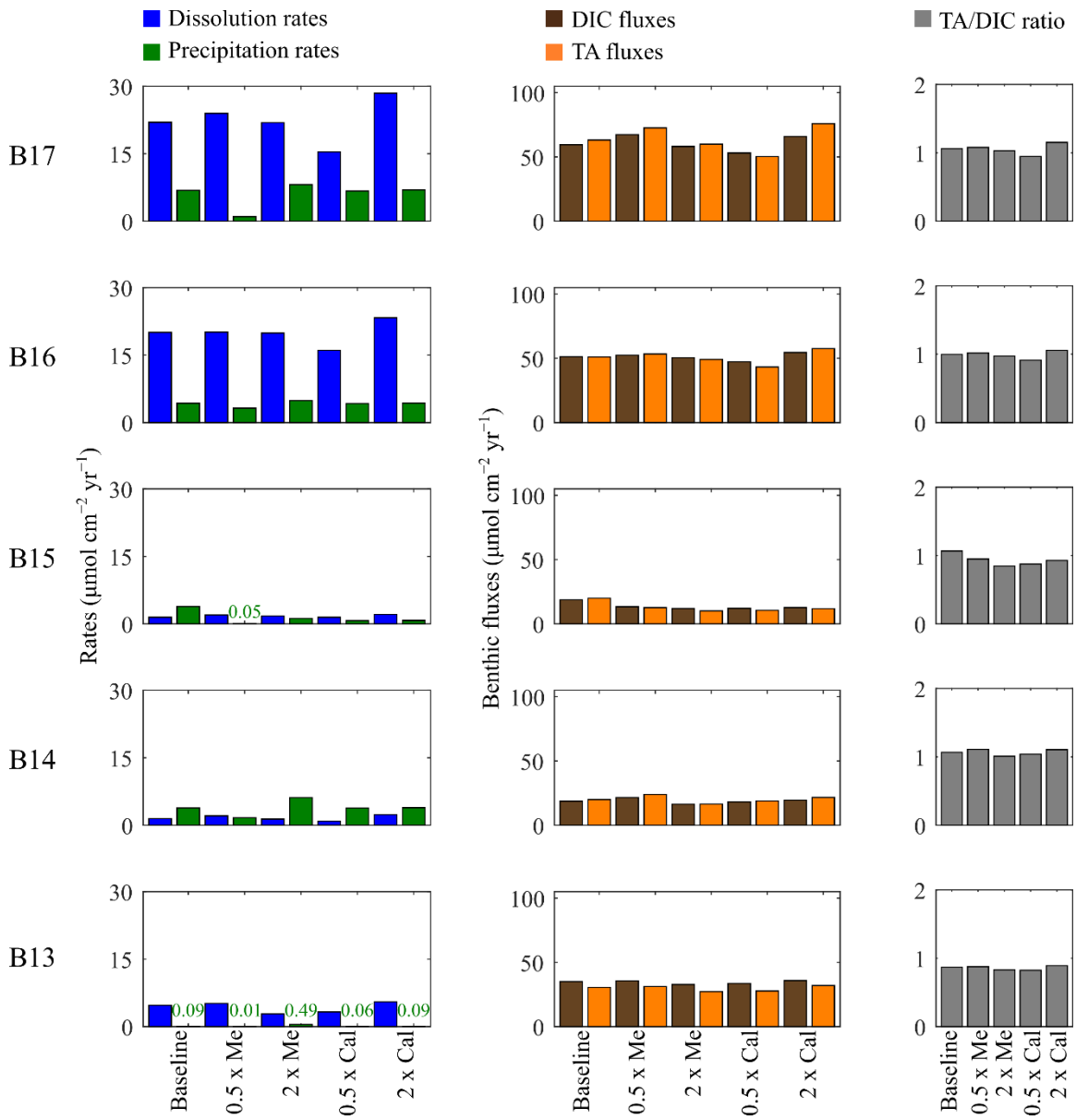

Figure S3. Sensitivity of seafloor carbonate chemistry parameters to changes in metal oxyhydroxides (halving and doubling) and calcite (halving and doubling) export relative to baseline conditions (see main text). Left column: rates of dissolution (blue) and precipitation (green). Middle column: benthic fluxes of DIC (brown) and TA (orange). Right column: buffering capacity (grey).

Tables

Table S2. Measured porewater pH in sediment cores (in cm below seafloor) from the Barents Sea 30°E South—North transect (B14—B17) in summer 2018 (see main text for details). At site B17, measurements were taken from three different coring deployments (i.e., R1—R3 are replicates).

Depth (cm)	B14	B15	B16	B17 (R1)	B17 (R2)	B17 (R3)
Bottom water	8.15	7.83	8.22	8.07	8.08	8.00
0.0	7.47	7.65	7.44	7.2	7.24	7.02
0.5	7.77	7.45	7.38	7.2	7.08	7.01
1.0	8.00	7.36	742	7.27	7.06	7.21
1.5	7.80	7.36	7.48	7.25	7.22	7.41
2.0	8.05	7.48	7.46	7.36	7.25	7.74
3.0	7.97	7.34	7.69	7.49	7.34	7.67
4.0	8.50	7.28	7.68	7.65	7.64	7.47
5.0	8.05	7.27	7.84	7.61	7.52	7.75
6.0	8.05	7.4	7.83	7.86	8.06	7.73
7.0	8.08	7.41		8.00	8.04	7.65
8.0	8.06	7.42		8.03	8.02	7.89
9.0		7.42			8.04	7.77
10.0		7.45				7.78

Table S3. Sensitivity analysis results for changes in particulate export to the seafloor at site B13. Rates (dissolution and precipitation) and benthic fluxes (dissolved inorganic carbon and total alkalinity) are integrated over the model domain (Sect. 2.2.4) and are given in µmol cm^{-2} yr^{-1}.

	Baseline	2.0 x Sed. rate	0.5 x TOC	2.0 x TOC	0.5 x Metals	2.0 x Metals	0.5 x Calcite	2.0 x Calcite
$R_{dissolution}$	4.7	4.6	3.2	3.6	5.2	2.8	3.3	5.5
$R_{precipitation}$	0.1	0.4	0.5	4.3	0.0	0.5	0.1	0.1
$J_{DIC,OM}$	30.4	48.5	15.2	60.8	30.4	30.4	30.4	30.4
$J_{DIC,Diss}$	4.7	4.6	3.2	3.6	5.2	2.8	3.3	5.5
$J_{DIC,Prec}$	−0.1	−0.4	−0.5	−4.3	0.0	−0.5	−0.1	−0.1
$J_{DIC,Total}$	35.1	52.7	17.9	60.2	35.6	32.8	33.6	35.8
$J_{TA,OM}$	19.1	40.3	5.9	69.9	19.3	19.8	19.1	19.1
$J_{TA,NH4}$	0.0	0.0	0.0	0.0	0.0	0.0	0.0	0.0
$J_{TA,Mn2+}$	−0.1	−0.1	0.0	−0.2	−0.1	−0.1	−0.1	−0.1
$J_{TA,Fe2+}$	−2.5	−3.5	−1.9	−4.1	−2.2	−3.9	−2.5	−2.4
$J_{TA,H2S}$	6.5	11.9	4.2	10.4	5.3	8.8	6.6	6.5
$J_{TA,Prec}$	−2.1	−6.0	−1.4	−14.9	−1.6	−3.0	−2.0	−2.1
$J_{TA,Diss}$	9.5	9.2	6.3	7.3	10.3	5.7	6.5	11.0
$J_{TA,Total}$	30.4	51.8	13.0	68.3	31.2	27.2	27.7	32.0
$\frac{J_{TA,Total}}{J_{DIC,Total}}$	0.87	0.98	0.73	1.13	0.88	0.83	0.82	0.89

Table S4. Sensitivity analysis results for changes in particulate export to the seafloor at site B14. Rates (dissolution and precipitation) and benthic fluxes (dissolved inorganic carbon and total alkalinity) are integrated over the model domain (Sect. 2.2.4) and are given in µmol cm^{-2} yr^{-1}.

	Baseline	2.0 x Sed. rate	0.5 x TOC	2.0 x TOC	0.5 x Metals	2.0 x Metals	0.5 x Calcite	2.0 x Calcite
$R_{dissolution}$	1.5	1.5	3.3	2.7	2.1	1.4	0.9	2.3
$R_{precipitation}$	3.9	8.2	0.6	20.6	1.7	6.1	3.8	3.9
$J_{DIC,OM}$	21.1	31.1	10.6	42.3	21.1	21.1	21.1	21.1
$J_{DIC,Diss}$	1.5	1.5	3.3	2.7	2.1	1.4	0.9	2.3
$J_{DIC,Prec}$	−3.9	−8.2	−0.6	−20.6	−1.7	−6.1	−3.8	−3.9
$J_{DIC,Total}$	18.7	24.5	13.3	24.4	21.6	16.4	18.2	19.6
$J_{TA,OM}$	23.2	38.7	5.4	85.3	25.7	22.1	23.2	23.2
$J_{TA,NH4}$	−0.1	−0.1	−0.1	−0.1	−0.1	−0.1	−0.1	−0.1
$J_{TA,Mn2+}$	−0.3	−0.2	−0.1	−0.2	−0.1	−0.3	−0.3	−0.3
$J_{TA,Fe2+}$	−4.3	−5.2	−1.9	−8.0	−4.7	−3.7	−4.3	−4.3
$J_{TA,H2S}$	7.1	13.0	3.6	6.1	4.2	8.6	7.1	7.1
$J_{TA,Prec}$	−8.6	−18.3	−1.3	−46.3	−5.2	−12.7	−8.6	−8.7
$J_{TA,Diss}$	2.9	3.1	6.6	5.5	4.2	2.7	1.8	4.7
$J_{TA,Total}$	20.0	30.8	12.1	42.2	23.9	16.5	18.9	21.7
$\frac{J_{TA,Total}}{J_{DIC,Total}}$	1.07	1.26	0.91	1.73	1.11	1.01	1.04	1.11

Table S5. Sensitivity analysis results for changes in particulate export to the seafloor at site B15. Rates (dissolution and precipitation) and benthic fluxes (dissolved inorganic carbon and total alkalinity) are integrated over the model domain (Sect. 2.2.4) and are given in µmol cm^{-2} yr^{-1}.

	Baseline	2.0 x Sed. rate	0.5 x TOC	2.0 x TOC	0.5 x Metals	2.0 x Metals	0.5 x Calcite	2.0 x Calcite
$R_{dissolution}$	1.8	1.5	1.4	1.9	2.0	1.8	1.5	2.1
$R_{precipitation}$	0.8	6.0	0.0	0.1	0.1	1.2	0.7	0.8
$J_{DIC,OM}$	11.4	18.6	5.7	22.8	11.4	11.4	11.4	11.4
$J_{DIC,Diss}$	1.8	1.5	1.4	1.9	2.0	1.8	1.5	2.1
$J_{DIC,Prec}$	−0.8	−6.0	0.0	−0.1	−0.1	−1.2	−0.7	−0.8
$J_{DIC,Total}$	12.5	14.1	7.1	24.6	13.3	11.9	12.1	12.7
$J_{TA,OM}$	9.1	18.0	3.5	22.0	9.0	9.3	9.1	9.1
$J_{TA,NH4}$	−1.7	−2.4	−0.9	−3.2	−1.7	−1.7	−1.7	−1.7
$J_{TA,Mn2+}$	−0.3	−0.6	−0.3	−0.4	−0.2	−0.4	−0.3	−0.3
$J_{TA,Fe2+}$	−2.9	−5.4	−1.1	−5.2	−2.5	−3.4	−2.9	−2.9
$J_{TA,H2S}$	5.5	12.5	2.2	9.5	4.8	5.8	5.5	5.5
$J_{TA,Prec}$	−2.0	−12.6	−0.2	−1.9	−0.7	−2.9	−2.0	−2.0
$J_{TA,Diss}$	3.7	3.1	2.9	3.9	4.0	3.5	2.9	4.2
$J_{TA,Total}$	11.3	12.5	6.0	24.7	12.7	10.1	10.6	11.8
$\frac{J_{TA,Total}}{J_{DIC,Total}}$	0.91	0.89	0.85	1.00	0.95	0.85	0.88	0.93

Table S6. Sensitivity analysis results for changes in particulate export to the seafloor at site B16. Rates (dissolution and precipitation) and benthic fluxes (dissolved inorganic carbon and total alkalinity) are integrated over the model domain (Sect. 2.2.4) and are given in µmol cm^{-2} yr^{-1}.

	Baseline	2.0 x Sed. rate	0.5 x TOC	2.0 x TOC	0.5 x Metals	2.0 x Metals	0.5 x Calcite	2.0 x Calcite
$R_{dissolution}$	20.0	17.5	17.7	14.3	20.1	19.9	16.0	23.3
$R_{precipitation}$	4.3	18.6	1.0	21.8	3.2	4.9	4.2	4.3
$J_{DIC,OM}$	35.5	52.0	17.7	71.0	35.5	35.5	35.5	35.5
$J_{DIC,Diss}$	20.0	17.5	17.7	14.3	20.1	19.9	16.0	23.3
$J_{DIC,Prec}$	−4.3	−18.6	−1.0	−21.8	−3.2	−4.9	−4.2	−4.3
$J_{DIC,Total}$	51.2	50.9	34.5	63.5	52.4	50.5	47.3	54.5
$J_{TA,OM}$	21.0	47.1	4.7	95.9	20.3	22.1	21.0	21.0
$J_{TA,NH4}$	−2.6	−1.9	−2.2	−1.9	−2.6	−2.6	−2.6	−2.6
$J_{TA,Mn2+}$	−4.1	−8.8	−0.5	−20.1	−3.6	−4.8	−4.1	−4.1
$J_{TA,Fe2+}$	−6.9	−11.9	−2.1	−11.5	−5.7	−7.9	−6.9	−6.9
$J_{TA,H2S}$	12.6	29.0	4.3	22.1	11.9	12.8	12.6	12.6
$J_{TA,Prec}$	−9.0	−37.3	−2.1	−46.0	−7.0	−10.1	−8.9	−9.1
$J_{TA,Diss}$	40.1	35.1	35.4	28.6	40.2	39.8	32.1	46.6
$J_{TA,Total}$	51.1	51.0	37.3	67.0	53.3	49.1	43.2	57.5
$\frac{J_{TA,Total}}{J_{DIC,Total}}$	1.00	1.00	1.08	1.06	1.02	0.97	0.91	1.06

Table S7. Sensitivity analysis results for changes in particulate export to the seafloor at site B17. Rates (dissolution and precipitation) and benthic fluxes (dissolved inorganic carbon and total alkalinity) are integrated over the model domain (Sect. 2.2.4) and are given in µmol cm^{-2} yr^{-1}.

	Baseline	2.0 x Sed. rate	0.5 x TOC	2.0 x TOC	0.5 x Metals	2.0 x Metals	0.5 x Calcite	2.0 x Calcite
$R_{dissolution}$	22.0	18.4	23.7	11.6	24.0	21.9	15.4	28.4
$R_{precipitation}$	6.9	22.4	1.8	13.6	1.0	8.1	6.7	7.0
$J_{DIC,OM}$	44.4	68.0	22.2	88.7	44.4	44.4	44.4	44.4
$J_{DIC,Diss}$	22.0	18.4	23.7	11.6	24.0	21.9	15.4	28.4
$J_{DIC,Prec}$	−6.9	−22.4	−1.8	−13.6	−1.0	−8.1	−6.7	−7.0
$J_{DIC,Total}$	59.5	64.1	44.0	86.7	67.3	58.2	53.1	65.8
$J_{TA,OM}$	47.1	87.2	9.2	166.9	44.2	48.8	47.1	47.1
$J_{TA,NH4}$	−1.3	−0.8	−1.9	−0.5	−1.3	−1.3	−1.3	−1.3
$J_{TA,Mn2+}$	−17.6	−26.9	−1.0	−53.1	−17.6	−19.4	−17.6	−17.6
$J_{TA,Fe2+}$	−13.9	−18.8	−4.9	−19.7	−8.7	−14.8	−14.0	−13.9
$J_{TA,H2S}$	19.2	38.0	7.5	18.7	12.0	19.5	19.2	19.2
$J_{TA,Prec}$	−14.2	−46.1	−3.8	−34.2	−3.8	−16.6	−13.9	−14.4
$J_{TA,Diss}$	44.0	36.9	47.3	23.2	47.9	43.8	30.8	56.9
$J_{TA,Total}$	63.1	69.3	52.4	101.3	72.6	59.9	50.2	75.9
$\frac{J_{TA,Total}}{J_{DIC,Total}}$	1.06	1.08	1.19	1.17	1.08	1.03	0.95	1.15

Additional Supporting Information (Files uploaded separately)

Table S1. Reaction network and parameters controlling the model-derived seafloor dynamics of pH and inorganic carbon in the Barents Sea. The terms x/y/z are defined as 106/12/1 (Freitas et al., 2020). The terms $\boldsymbol{t_a^i}$, $\boldsymbol{t_c^i}$, and $\boldsymbol{t_s^i}$ denote the mass action laws and stoichiometric coefficients of total alkalinity, total dissolved inorganic carbon, and total sulfides, respectively (e.g., Blouet et al., 2021; Jourabchi et al., 2005). The terms ΔDIC and ΔTA denote the stoichiometric coefficients of production (positive) and consumption (negative) of benthic-pelagic fluxes of dissolved inorganic carbon and total alkalinity, respectively. $\boldsymbol{\gamma_N}$ = 1/12 and $\boldsymbol{\gamma_P}$= 1/106 (e.g., Soetaert et al., 2007). SD is the volume conversion term ($\boldsymbol{SD} = \frac{\boldsymbol{1-porosity}}{\boldsymbol{porosity}}$) (e.g., Freitas et al., 2020).

References

Blouet, J.-P., Arndt, S., Imbert, P., & Regnier, P. (2021). Are seep carbonates quantitative proxies of CH4 leakage? Modeling the influence of sulfate reduction and anaerobic oxidation of methane on pH and carbonate precipitation. *Chemical Geology*, *577*, 120254. https://doi.org/10.1016/j.chemgeo.2021.120254

Freitas, F. S., Hendry, K. R., Henley, S. F., Faust, J. C., Tessin, A. C., Stevenson, M. A., Abbott, G. D., März, C., & Arndt, S. (2020). Benthic-pelagic coupling in the Barents Sea: An integrated data-model framework. *Philosophical Transactions of the Royal Society A: Mathematical, Physical and Engineering Sciences*, *378*(2181), 20190359. https://doi.org/10.1098/rsta.2019.0359

Jourabchi, P., Van Cappellen, P., & Regnier, P. (2005). Quantitative interpretation of pH distributions in aquatic sediments: A reaction-transport modeling approach. *American Journal of Science*, *305*(9), 919–956. https://doi.org/10.2475/ajs.305.9.919

Soetaert, K., Hofmann, A. F., Middelburg, J. J., Meysman, F. J. R., & Greenwood, J. (2007). The effect of biogeochemical processes on pH. *Marine Chemistry*, *105*(1–2), 30–51. https://doi.org/10.1016/j.marchem.2006.12.012